95247X

A Study of the Free Oscillations of the Earth

GORDON J. F. MACDONALD AND NORMAN F. NESS

National Aeronautics and Space Administration
Theoretical Division, Goddard Space Flight Center
Washington, D. C.

Abstract. Published observations on the toroidal oscillations of the earth are critically reviewed. A supplementary analysis of the record obtained by the Lamont strain seismometer is presented. Eleven toroidal modes are identified, and it is concluded that the periods are known to within 1 per cent.

A perturbation scheme involving the ratio of the angular velocity of the earth to the resonant frequency is used in calculating the effects due to the rotation of the earth on the resonant frequency. The free oscillations are viewed as a superposition of traveling waves. In a nonrotating system two traveling waves combine to produce a stationary standing wave. In a rotating system, the rotation distinguishes between waves that travel in the direction of rotation and those that travel in the opposite direction. Rotation removes a degeneracy and results in a splitting of a spectral peak of order l into $2l + 1$ peaks. The fractional displacement in frequency for the lowest-order toroidal oscillations is 1/206 and of the same order as the Q of the peak, so that splitting will probably not be observed in the toroidal oscillations. Viewed locally, rotation causes a particle to precess about a direction parallel to the axis of rotation. This precession will cause a variation of amplitude with time if the motion is recorded by an instrument with an anisotropic response function. Care is therefore needed in studying the time decay of a given spectral peak. Rotation also couples the normal coordinates so that a motion that is initially purely horizontal will develop a vertical component. It is expected that vertical seismometers should record particle motion with the toroidal frequencies.

The perturbations of the toroidal oscillations due to core-mantle interaction are treated in detail. An exact expression is obtained for the rate of energy dissipated by a finitely conducting plate oscillating across a magnetic field. The energy dissipated at the core-mantle boundary due to viscous and hydromagnetic coupling is shown to be insignificant as compared with the energy dissipated within the mantle. The toroidal magnetic field leaking into the lower mantle combines with the dipole field, resulting in a stress on the mantle, tending to stiffen the lower boundary. The stress is of sufficient magnitude to produce a displacement toward higher frequency in the lower-order toroidal oscillations. Observations on the $_0T_2$ oscillations lead to an estimate of the toroidal magnetic field in the lower mantle.

A calculation of elastic energy in the low-order oscillations suggests a value of 10^{18} ergs/cph for the energy density at low frequencies in the Chilean earthquake. Each mode of oscillation has a characteristic radial distribution of elastic energy associated with it. This distribution determines which parts of the earth contribute most heavily in determining a particular resonant frequency. The distribution of energy for the lower 17 modes for a homogeneous and a Gutenberg model earth is calculated. The resonant frequencies for models of the earth based on the Gutenberg and Lehmann distribution of elastic properties are presented. It is shown that the Gutenberg model earth fits the observations more closely than the Lehmann model and that a slight alteration of the Gutenberg model gives a significantly better fit to the observations. The alteration involves a lower shear-wave velocity in the lower mantle while the Gutenberg velocity distribution is maintained in the upper mantle.

Various studies of the earth's oscillations coupled with surface-wave investigations substantiate Gutenberg's hypothesis of a layer of low velocity in the upper mantle. The physical conditions required for the formation of a region of low velocity are examined in detail. The results confirm Birch's earlier statement that a temperature gradient in excess of 6° to 7°/km is needed to produce a decrease in velocity. The low-velocity layer does not require that the temperature approach or exceed the melting temperature. If the upper mantle is homogeneous, the region of lower velocity should commence at the base of the crust and extend to 150 km under the oceans and about 100 km under continental regions. The distribution of thermal conductivity and radioactivity consistent with the low-velocity layer is also considered.

MacDONALD AND NESS

FREQUENTLY USED SYMBOLS

$B^m_{i,l}$ $C^m_{i,l}$ $P^m_{i,l}$ vector spherical harmonics of angular order l, m.

C_A Alfvén wave phase velocity, part 4.

C_S shear-wave phase velocity.

C_P longitudinal-wave phase velocity.

$_nE_l$ total elastic energy of toroidal oscillation of radial order n, angular order l, part 5.

H_i magnetic field intensity, part 4.

K kinetic energy, part 3.

K_R kinetic energy relative to rotating coordinate system, part 3.

K_S adiabatic incompressibility, part 7.

K_T isothermal incompressibility, part 7.

$_nQ_l$ dimensionless measure of sharpness of resonance peak of oscillation of angular order l, radial order n, part 5.

$_nS_l^m$ spheroidal mode of oscillation, introduction.

$_nT_l^m$ toroidal mode of oscillation, introduction.

j_l spherical Bessel function of first kind, part 2. (j_i is current density, part 4.)

X_l^m complex surface spherical harmonic.

f frequency in cycles per unit time; as subscript referring to fluid.

Δf half-power bandwidth of resonance peak, part 3.

i, j, k, s, t tensor subscripts; summation convention applied.

l, m integer denoting angular order of spherical harmonic; summation convention does not apply.

n integer denoting order of oscillation associated with coordinate r.

p hydrostatic pressure, part 2.

p_{ij} stress tensor, part 2.

q_i complex amplitude of particle displacement, part 2.

u_i particle displacement, part 2.

y_l spherical Bessel function of second kind, part 2.

α dimensionless parameter, part 4; thermal expansion, part 7.

β dimensionless parameter, part 4; isothermal compressibility, part 7.

δ electromagnetic skin depth, part 4.

δ_ν viscous boundary layer thickness, part 4.

δ_{ij} Kronecker delta.

ϵ Ω/ω parts 2, 3; displacement associated with critical Maxwell stress, part 4.

ϵ_{ij} elastic strain tensor, part 5.

ϵ_{ijk} alternating tensor.

η electromagnetic viscosity, part 5.

λ lamé constant, part 2; dimensionless parameter, part 4.

μ rigidity, parts 2, 7; magnetic permeability, part 4.

ν kinematic viscosity, part 4.

σ electrical conductivity, part 4.

ρ density.

τ_{ij} elastic stress tensor, part 2.

ω angular frequency.

ψ_r Elastic energy per unit radius associated with radial stress, part 5.

ψ_θ elastic energy per unit radius associated with conical stress, part 5.

Ω angular velocity of rotation.

INTRODUCTION

The observations of the free oscillations of the earth excited by the great Chilean earthquake of May 22, 1960, permit the application of new methods to the study of the earth's interior. The properties of the earth as a whole combine to determine the resonant frequencies. The separation of the relative contributions of parts of the earth in determining the resonant frequencies poses formidable problems, the solution of which will provide new restraints on speculation regarding the earth's interior.

The free vibrations of a nonrotating elastic sphere can be classified into two groups: the torsional or toroidal[1] oscillations are those in which a particle executes motion on a spherical surface; there is no radial component of the motion. The toroidal oscillations combine to form the familiar horizontally polarized shear waves of classical seismology. The spheroidal oscillations involve both radial and tangential motion. The rotation of the earth introduces interesting complications into the particle motions, coupling the toroidal and spheroidal modes. However, to an approximation determined by the ratio of the angular velocity of rotation of the earth to the resonant frequency, the coupling effect of rotation can be neglected.

[1] Toroidal is used throughout the paper in preference to torsional, for two reasons: toroidal, like spheroidal, has a purely geometric connotation, whereas torsional implies stress; toroidal is familiar from its use in the classic works on geomagnetism and the vector Helmholtz equation by *Bullard and Gellman* [1954] and *Elsasser* [1956].

The spectrum of a seismic disturbance is characterized by sharp peaks for periods between an hour and about 10 minutes. At higher frequencies the isolated peaks merge into a continuum as a result of the finite Q of the earth and the increased number of peaks. At frequencies for which the spectrum is recognizably discrete, the normal modes involve a major part of the earth. The characteristic length associated with these vibrations is large compared with the inhomogeneities of the continent-ocean system. Hence, it is customary to assume spherical symmetry for the earth. The solution to the equations of vibration of the earth is separated into a function dependent upon radius and a function dependent on the angular coordinates. The angular function is written as a sum of surface spherical harmonics, $X_l{}^m$.

$$X_l{}^m = P_l{}^m(\cos\,\theta)\,e^{im\varphi} \qquad (1)$$

$P_l{}^m$ is the associated Legendre function; l and m are the integers denoting the order of the spherical surface harmonic with respect to the angular coordinates θ and φ. The integers l and m determine the surface pattern of deformation associated with a particular free oscillation. The number of lines of vanishing displacement associated with the angular coordinate θ is $l - |m|$; the number of nodal lines associated with angular coordinate φ is $2m$. There will also be nodal surfaces associated with the radial function. A free oscillation can thus be characterized by three integers, l and m determining the pattern of displacement on a spherical surface, and n determining the number of radial nodal surfaces. The notation we propose is

$$_nS_l{}^m \qquad _nT_l{}^m$$

for the spheroidal and toroidal oscillations, respectively. $_nT_l{}^m$ denotes a toroidal oscillation with n radial nodal surfaces and a displacement pattern on the surface of the sphere determined by l and m.

Numerical treatment of the toroidal oscillations is markedly simpler than that of the spheroidal oscillations. The set of three second-order coupled differential equations describing elastic vibrations reduces to a single second-order differential equation in the case of the toroidal oscillations. This mathematical simplification arises from the fact that the toroidal oscillations do not perturb the earth's density or

gravitational field. The mathematical simplicity of the toroidal oscillations does not dispose of their inherent geophysical interest. The toroidal oscillations involve only shear motions and are confined to the mantle of the earth. The knowledge of their resonant frequencies can be used in determining the distribution of shear-wave velocity within the mantle. In addition, the resonant frequencies depend on the boundary condition at the core-mantle boundary, so that study of the toroidal oscillations can yield information on the nature of the core-mantle boundary.

The present study is an attempt to obtain geophysically significant information about the interior of the earth from the observations of the toroidal oscillations. The observations now available are sufficient to settle certain problems, but answers to many other questions will depend on more detailed observations. The resonant frequencies for the toroidal modes are not as well known as those for the spheroidal modes. The toroidal oscillations appear to have been excited to a lesser degree by the Chilean earthquake than the spheroidal oscillations. That is the present situation; we expect that in the future the toroidal oscillations will be more clearly delineated.

Part 1 reviews the published observations on the toroidal oscillations. In addition, a new analysis is presented of the record obtained by the Lamont strain seismograph. The equations of motion are introduced in part 2. The separation of the effects due to the rotation of the earth is accomplished by means of a perturbation scheme involving the ratio of the angular velocity of the earth to the resonant frequency. The explicit effects of rotation on the motion are taken up in part 3. Viewed locally, a particle precesses about a direction parallel to the axis of rotation. Rotation couples the normal coordinates so that a motion that is initially purely horizontal will develop a vertical component. An explicit expression is obtained for the magnitude of the shift in resonant frequency due to rotation.

The resonant frequencies of the lowest-order toroidal oscillations depend on the nature of the core-mantle coupling; the general problem of core-mantle interaction is considered in part 4. The toroidal field leaking from the core into the lower mantle may stiffen the lower boundary

enough to produce a perturbation in the gravest toroidal oscillation. Dissipation results from the viscous and hydromagnetic coupling. In part 5 the radial distribution of energy and the total energy associated with any one mode of oscillation are considered. The calculation of the total elastic energy in any mode of oscillations leads to an estimate of the energy density in the Chilean earthquake. Calculations of the resonant frequencies of specific models of the earth are taken up in part 6. A slight modification of the Gutenberg model earth leads to resonant frequencies in close agreement with observations. The observed toroidal frequencies are consistent with an earth model having a low-velocity zone. The physical conditions producing a low-velocity zone are treated in part 7. If the upper mantle is homogeneous on a large scale, the low-velocity layer should commence at the base of the crust and extend to depths of 150 km under oceanic regions and about 100 km under continental regions.

In order to interpret the earth's free oscillations properly, some physical feeling must be developed for the oscillations of an inhomogeneous, rotating, nearly elastic body. The present study is an attempt to provide an introduction to the toroidal oscillations. A comparable treatment of the spheroidal oscillations is possible but will involve numerical computations of a higher degree of complexity.

1. OBSERVATIONS OF THE TOROIDAL OSCILLATIONS

The low-frequency toroidal oscillations have been observed by *Alsop, Sutton, and Ewing* [1961a] and by *Benioff, Press, and Smith* [1961]. In these studies, the oscillations excited by the Chilean earthquake of May 22, 1960, were recorded both by Benioff strain seismometers and by pendulum seismographs. Alsop and co-workers report results from both instruments; Benioff and co-workers describe results obtained using strain seismometers located at Isabella in California and Naña in Peru. In both studies the analog records were digitized and Fourier-analyzed. The Lamont records were first low-pass-filtered by taking running averages over 19 and 21 points and then decimated, using every third point in the case of the pendulum instrument and every fifth point in the case of the strain instruments. The data were then subjected to a standard Fourier analysis. The results are listed in Table 1, the identification of the modes being that given by Alsop and collaborators. This depends upon a comparison with the theoretical calculations of the frequency of toroidal oscillations.

Benioff and his collaborators carried out a similar analysis. Their strain-seismometer records were subjected to low-pass filtering by smoothing by threes, fives, and sevens and then decimated by taking every third point. In addition, tides and other low-frequency phenomena were removed by a high-pass filter. The resultant records were subjected to a power spectral analysis by the methods developed by *Blackman and Tukey* [1958]. The results obtained by Benioff and his co-workers are listed in Table 1. The theoretical results of *Gilbert and MacDonald* [1960] were used in identifying the spectral peaks.

Through the courtesy of Alsop, Sutton, and Ewing, we obtained a set of the digitized records

TABLE 1. Observed Periods in Minutes of the Toroidal Oscillations

Mode of Oscillation	Analysis of Lamont Strain	Lamont Strain	Lamont N-S Pendulum	Lamont E-W Pendulum	Isabella Strain
$_0T_2$	44.75	44.80		43.98	42.3
$_0T_3$	28.57	28.48	28.43	28.68	28.6
$_0T_4$	21.95	21.90	21.83	21.62	21.8
$_0T_5$	18.02	17.81	17.85	17.87	17.9
$_0T_6$	15.51		15.10		15.5
$_0T_7$	13.75		13.30	13.28	13.5
$_0T_8$	12.35	12.10	12.08	12.25	12.3
$_0T_9$	11.24	11.24	11.02	10.98	11.21
$_0T_{10}$	10.33				10.33
$_0T_{11}$	9.614				9.60
$_0T_{12}$	9.065				
$_0T_{14}$	7.985				

of the Lamont strain seismometer covering a period of 36 hours with data points taken at intervals of 26.55 seconds. We have analyzed the record by techniques identical to those employed by *Ness, Harrison, and Slichter* [1961] in their analysis of the spheroidal modes as recorded by the UCLA tidal gravimeter. The data were first subjected to a 101-point low-pass filter designed by *Martin* [1957], and the record was then decimated by taking every other point. The half-power point for the filter after decimation corresponded to a frequency of 14 cph. The data were then subjected to a double-stage Chebyshev high-pass filter. The half-power point of this filter corresponds to a frequency of 0.9 cph. For the frequencies passed there is a total 3 per cent ripple about unity. The records were also Fourier-analyzed applying a Chebyshev time window with the side lobe level fixed at 0.01 of the main lobe. The results of the analysis are shown in Table 1. The peaks were identified by comparison with the theoretical calculations of *Gilbert and MacDonald* [1960]. Additional assistance in the identification of the modes was provided by detailed comparison with the spheroidal modes observed on the UCLA gravimeter [*Ness, Harrison, and Slichter*, 1961]. Peaks that were weak or absent on the gravimeter records were identified as corresponding to the toroidal modes. This procedure is possible since the gravimeter records solely the vertical motion whereas the strain seismometer responds to both vertical and horizontal motion. The conversion of toroidal motion into a vertical motion by rotational coupling introduces some uncertainty in this identification (see part 3).

The mode $_0T_2$ does not show up as a well-defined peak on the Lamont strain record, but is well above noise level with a period of 42.3 minutes in the records obtained by Benioff and collaborators at Naña and Isabella. Both the Isabella and Lamont strain instruments were within 8° of the nodal line for $_0T_2$ (see part 5).

The discrepancy between the period obtained for $_0T_5$ in our analysis and in the analysis of Alsop, Benioff, and their co-workers is considered to be due to improper identification. The gravimeter shows a split peak at 17.68/17.88 minutes, corresponding to the spheroidal oscillation $_1S_3$. The Lamont listing of the observed peaks includes an unidentified peak at 18.0 minutes. This corresponds to the $_0T_5$ oscillation,

and the peak listed as the $_0T_5$ oscillation must then be $_1S_3$. The modes $_0T_7$ and $_0T_8$ similarly appear to be incorrectly identified, owing to their close proximity to spheroidal modes as detected by the gravimeter.

2. EQUATIONS OF MOTION

The numerical methods used in obtaining the resonant frequencies of an inhomogeneous earth require the solution to the equations of motion for a homogeneous spherical elastic shell. The solution is well known and is discussed by *Morse and Feshbach* [1953], *Love* [1927], *Alterman, Jarosch, and Pekeris* [1959], and *Gilbert and MacDonald* [1960]. In this section we review the general theory of oscillation in an inhomogeneous sphere in order to introduce a notation and a perturbation scheme and establish a number of subsidiary results. The theory is specialized to the case of a homogeneous shell at a number of points.

We consider a rotating isotropic elastic solid. The equation of motion referred to a coordinate system fixed to the mean body is

$$\rho \frac{\partial^2 u_i}{\partial t^2} + 2\rho\epsilon_{ijk}\Omega_j \frac{\partial u_k}{\partial t}$$
$$= -\rho \frac{\partial}{\partial x_i} \{ U(r) + \tfrac{1}{2}[\Omega_i(x_i + u_i)]^2$$
$$- [\Omega_i^2(x_k + u_k)^2]\} + \frac{\partial}{\partial x_j} p_{ij}$$
$$U^1 = U(r) + \tfrac{1}{2}[\Omega_i(x_i + u_i)]^2$$
$$- \tfrac{1}{2}\Omega_i^2(x_k + u_k)^2$$

provided that we neglect electromagnetic forces and dissipation and assume that the strains are small. u_i is the displacement vector; Ω_j is the angular velocity of rotation of the coordinate system and is assumed constant. $U(r)$ is the spherically symmetric potential of the gravitational forces. The term on the right-hand side involving the angular velocity represents the cylindrically symmetrical centrifugal potential. The stress tensor p_{ij} may be written

$$p_{ij} = -p \, \delta_{ij} + \tau_{ij}$$

where p is the hydrostatic pressure and τ_{ij} is the elastic stress tensor measured from the compressed equilibrium state.

In a homogeneous elastic material the diver-

gence of the elastic stress tensor is

$$\frac{\partial \tau_{ij}}{\partial x_j} = (\lambda + u) \frac{\partial^2 \mu_j}{\partial x_i \, \partial x_j} + \frac{\partial^2 u_i}{\partial x_j^2}$$

where λ and μ are Lamé constants.

The equations of motion referred to a rotating system of reference axes differ from the usual equations in two terms. The term on the right-hand side involving the angular velocity is the ordinary centrifugal force. The term involving velocity on the left-hand side also depends on the angular velocity and is the Coriolis or gyroscopic force. The effect of this term is to couple motion along the various coordinate axes. The equations might also be written in terms of the principal or normal coordinates. Then, if the potential energy is written as a sum of square terms, a change in one of the normal coordinates brings about a change in the remaining coordinates because of the gyroscopic terms. The rotational coupling introduces a complexity in the motion that is of considerable importance in the interpretation of the observations of the earth's free oscillations.

The time variation of the displacement is assumed to be of the form

$$u_i = q_i e^{i \omega t}$$

where ω is the angular frequency of vibration and q_i is the complex amplitude. In terms of the complex amplitude and frequency, the equations of motion are

$$-\omega^2 \rho q_k + 2i\rho\omega\epsilon_{kst}\Omega_s q_t$$
$$= -\rho \frac{\partial}{\partial x_k} U^1 + \frac{\partial p_{ki}}{\partial x_i} \quad (2)$$

Let

$$\epsilon = \Omega/\omega_0$$

and we note that the gyroscopic terms in equation 2 are of order ϵ, the centrifugal force of order ϵ^2. Since the fundamental frequency of the oscillations is of the order of an hour, ϵ is always small compared with unity. This suggests a perturbation scheme of the form

$$q_i = q_i^0 + \epsilon q_i^1 + \epsilon^2 q_i^2 + \cdots \quad (3)$$

$$\omega = \omega_0(1 + \alpha_1\epsilon + \alpha_2\epsilon^2 + \cdots) \quad (4)$$

The equations of motion to zero order and first order in ϵ are then

$$-\rho\omega_0^2 q_k^0 + \rho \frac{\partial}{\partial x_k} U_0^1 - \frac{\partial p_{ki}^0}{\partial x_i} = 0 \quad (5)$$

$$-\rho\omega_0^2 q_k^1 + \rho \frac{\partial}{\partial x_k} U^1 - \frac{\partial p_{ki}^1}{\partial x_i}$$
$$= -2\rho\omega_0^2\alpha_1 q_k^0 + 2i\rho\omega_0^2\epsilon_{kst}z_s q_t^0 \quad (6)$$

$$\Omega_i = \Omega z_i$$

The only practical method of obtaining a solution to equation 5 is to utilize a series expansion. A solution that takes full advantage of the spherical symmetry is

$$q_i = \sum_{l=0}^{\infty} \sum_{m=-l}^{l} [\sqrt{l(l+1)}C_{i,l}^m(\theta, \varphi) \, _nW_l(r)$$
$$+ P_{i,l}^m \, _nU_l(r) + \sqrt{l(l+1)}B_{i,l}^m \, _nV_l(r)]$$

where the vector spherical harmonics [*Morse and Feschbach*, 1953; *Stratton*, 1941] are defined by

$$C_{i,l}^m = \frac{1}{\sqrt{l(l+1)}} \epsilon_{ijk} \frac{\partial}{\partial x_j} (x_k X_l^m)$$

$$P_{i,l}^m = \frac{x_i}{r} X_l^m$$

$$B_{i,l}^m = \frac{1}{\sqrt{l(l+1)}} r \frac{\partial}{\partial x_i} X_l^m$$

X_l^m are the complex spherical harmonics. It should be noted that in the notation adopted the letters l and m are reserved for the angular order of the spherical harmonics and are associated with the colatitude θ and longitude φ, respectively. The coordinate subscripts are separated from the order subscripts by a comma; the comma does not signify differentiation. The subscript n in the radial functions denotes the radial order or the number of zeros in the radial function. In the following the vector $C_{i,l}^m$ plays an important role. In Cartesian coordinates, C_i has the components

$$\sqrt{l(l+1)}C_{1,l}^m = (\tfrac{1}{2})(1 - \delta_{0m})(n + m)$$
$$\cdot (n - m + 1)iX_l^{m-1} + (\tfrac{1}{2})(1 + \delta_{0m})iX_l^{m+1}$$

$$\sqrt{l(l+1)}C_{2,l}^m = (\tfrac{1}{2})(1 - \delta_{0m})(n + m)$$
$$\cdot (n - m + 1)iX_l^{m-1} - (\tfrac{1}{2})(1 + \delta_{0m})iX_l^{m+1}$$

$$\sqrt{l(l+1)}C_{3,l}^m = -miX_l^m \quad (7)$$

provided that x_3 is taken as the axis of the spherical harmonic X.

The vectors C_i, P_i, B_i are mutually orthogonal. The motions described by

$$q_i = \sum_{l=0}^{\infty} \sum_{m=-l}^{l} \sqrt{l(l+1)} C^m_{i,l} (\theta, \varphi) \cdot {}_n W_l(r) \qquad (8)$$

involve no radial component; the particles remain on a spherical surface. The density remains constant since

$$\partial q_i / \partial x_i = 0$$

The motion is that of a horizontally polarized shear wave and represents the toroidal oscillations. In a homogeneous elastic shell the equation of motion to zero order in ϵ is

$$\rho \omega_0^2 q_k^{\,0} + \mu(\partial^2 q_k^{\,0} / \partial x_i^{\,2}) = 0 \qquad (9)$$

since the rigidity μ is constant throughout the spherical shell. The explicit solution to equation 9 is [Gilbert and MacDonald, 1960]

$$q_k = \sum_{l=1}^{\infty} \sum_{m=-l}^{l} \sqrt{l(l+1)} C^m_{k,l} \cdot [{}_n A_l^{\,m} j_l(kr) + {}_n B_l^{\,m} y_l(kr)]$$

where j_l and y_l are the spherical Bessel functions of the first and second kind. k is the wave number

$$k = \omega \sqrt{\rho/\mu}$$

The resonant frequencies for the toroidal modes are obtained by substituting the solution (equation 8) into the appropriate boundary conditions. We note that the modes are degenerate in m. The normal modes can be considered as a superposition of traveling waves. For a given l each pair of m values corresponds to two traveling waves: one travels in the direction of increasing Q, the other in the opposite direction. In a nonrotating system the two waves travel at the same speed to give a pattern of surface displacement that remains constant with time. The modes of different m correspond to the same energy in a nonrotating system. The degeneracy in m allows a considerable simplification. We set $m = 0$ and obtain for the toroidal displacements

$$q_r = 0$$

$$q_\theta = 0$$

$$q_\varphi = \sum_{l=0}^{\infty} P_l^{\,1}(\cos \theta)_n W_l(r)$$

3. Effect of Rotation on Toroidal Oscillations

The effect of rotation on the toroidal oscillations can be readily understood in a qualitative fashion. For toroidal motion, the solution to the zero-order equation 5 is

$$u_\theta = \sum_{l=0}^{\infty} \sum_{m=-l}^{l} \frac{im}{\sin \theta} P_l^{\,m} {}_n W_l(r) \cdot \exp [i(m\varphi + \omega_l^{\,m} t)]$$

$$u_\varphi = \sum_{l=0}^{\infty} \sum_{m=-l}^{l} (P_l^{\,m+1} - m \cot \theta P_l^{\,m}) {}_n W_l(r) \cdot \exp [i(m\varphi + \omega_l^{\,m} t)]$$

As was noted above, the modes are degenerate in m. In the degenerate case the two traveling waves associated with a pair ($+$ and $-$) of m numbers combine to give a stationary standing wave. Consider the case of rotation where the axis of rotation and the pole of the surface spherical harmonic coincide. For a given m one of the associated pair of traveling waves is carried along by the rotation whereas the other is retarded by the rotation. We should then expect that the rotation should remove degeneracy with respect to the wave number m. The rotation distinguishes between traveling waves that have a positive m and those that have a negative m. The removal of the degeneracy in the case of toroidal oscillations is particularly simple and will be dealt with in detail in this section. We first examine the effect of rotation on the particle motion and then consider the field equations.[2]

As an introduction to the effect of rotation on the toroidal oscillations we approximate the equation of motion

$$\rho \frac{\partial^2 u_i}{\partial t^2} - \mu \frac{\partial^2 u_i}{\partial x_k^{\,2}} = 0$$

[2] Backus and Gilbert [1961] have presented a detailed treatment of the rotational splitting of the normal modes. A solution has also been obtained by Alterman and Pekeris (private communication).

PATH WITH NO ROTATION

PATH WITH ROTATION
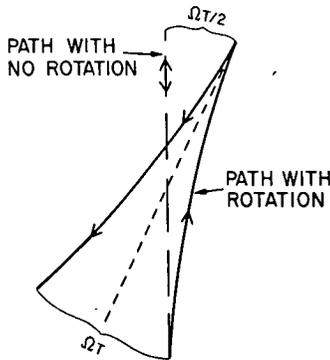
Fig. 1. Motion of a vibrating particle in a plane rotating at angular velocity Ω.

by

$$\frac{d^2 u_i}{dt^2} + \omega_0{}^2 u_i = 0$$

where ω_0 is the resonant frequency for a particular l in the absence of rotation. We further assume that the initial vibration is in a plane perpendicular to the axis of rotation, and we set the axis of rotation parallel to the x_3 axis. The equations of motion in the rotating plane are then

$$\frac{d^2 u_1}{dt^2} + \omega^2 u_1 = -2\Omega \frac{du_2}{dt} \qquad (10)$$

$$\frac{d^2 u_2}{dt^2} + \omega^2 u_2 = 2\Omega \frac{du_1}{dt} \qquad (11)$$

Multiplying equation 11 by i and adding to equation 10 we obtain

$$\left(\frac{d^2}{dt^2} + 2i\Omega \frac{d}{dt} + \omega^2\right) Z = 0 \qquad (12)$$

where $Z = u_1 + iu_2$. In equations 10 and 11 we neglect terms involving the square of the angular velocity of rotation. For an angular velocity of rotation less than the frequency of vibration, the solution of (12) is

$$Z = \exp(-i\Omega t)$$

$$\cdot [A_1 \exp(i\omega t) + A_2 \exp(-i\omega t)] \qquad (13)$$

$$u_1 + iu_2 = (u_1{}^0 + u_2{}^0) \exp(-i\Omega t)$$

$u_1{}^0$ and $u_2{}^0$ are the components of vibration in the absence of rotation. The effect of rotation is to turn the path of vibration about the vertical with angular velocity Ω. The motion is similar

to that of a Foucault pendulum. The horizontal plane of the motion is shown in Figure 1, where T is the period of the oscillation in the absence of rotation.

Figure 2 illustrates a vibration along the line OA with an amplitude A. The axis of rotation is taken as the x_3 axis. In a coordinate system rotating with angular velocity Ω about x_3, the particle will oscillate with frequency ω_0 and amplitude A along the line OA and precess around the x_3 axis at a rate Ω, tracing out a right circular cone. The Cartesian components of the motion are then

$$u_1 = A \cos \omega_0 t \sin \psi \cos \Omega t$$

$$u_2 = A \cos \omega_0 t \sin \psi \sin \Omega t$$

$$u_3 = A \cos \omega_0 t \cos \psi$$

where the displacement in the absence of rotation is

$$u_1 = A_1 \cos \omega_0 t$$

Making the substitutions

$$A \sin \psi = 2B \qquad A \cos \psi = 2C$$

The displacement can be written as the sum of three vectors

$$u_1 = a_1 + b_1 + c_1$$
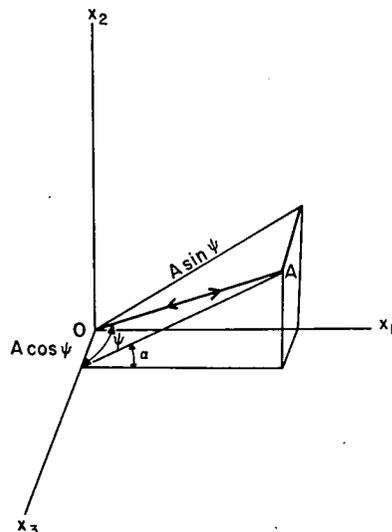
Fig. 2. Particle vibrating along OA and precessing about x_3.

where

$$a_1 = B \cos (\omega_0 + \Omega) t.$$

$$a_2 = B \sin (\omega_0 + \Omega) t.$$

$$a_3 = 0.$$

$$b_1 = B \cos (\omega_0 - \Omega) t.$$

$$b_2 = B \sin (\omega_0 - \Omega) t.$$

$$b_3 = 0.$$

$$c_1 = c_2 = 0.$$

$$c_3 = c \cos \omega_0 t.$$

The vector a_1 is located in the x_1-x_2 plane and rotates about the x_3 axis in a positive sense with frequency $\omega_0 + \Omega$. The vector b_1 is in the same plane and rotates about the x_3 axis in a negative sense with a frequency $\omega_0 - \Omega$. The rotation therefore resolves the original linear oscillation into three components whose amplitude depends on the angle between the axis of rotation and the direction of oscillation. The component of the vector parallel to the axis of rotation is unaffected by the rotation; the other two components have displaced frequencies.

The above discussion neglects the coupling produced by the rotation. In order to illustrate this, we approximate the particle motion by a harmonic oscillator. The x_1-x_2 plane is tangent to the spherical surface with the x_3 axis along the vertical. It is assumed that a particle vibrates in the x_1-x_2 plane with the frequency ω_T in the absence of rotation. The particle can also vibrate along the x_3 direction with the frequency ω_S. ω_T represents a particular toroidal oscillation, and ω_S represents a spheroidal oscillation. The particle is set into oscillation, and in the absence of rotation the motion is

$$u_1{}^0 = A_1 e^{i\omega_T t} + B_1 e^{-i\omega_T t}$$
$$u_2{}^0 = A_2 e^{i\omega_T t} + B_2 e^{-i\omega_T t} \qquad (14)$$

Relative to a rotating coordinate system, the equation can be dealt with using the perturbation scheme in terms of the parameter ϵ. (See equations 3 and 4.) The motion in the x_1-x_2 plane, to the first order in ϵ, is given by equation 13. For the u_3 componen t the solution to zero order in ϵ is $u_3{}^0 = 0$, since initially there is no displacement in the x_3 direction. To first order in ϵ the

equation for the u_3 component is

$$\frac{\partial^2 u_3}{dt^2} + \omega_s{}^2 u_3 = \Omega_1 \frac{\partial u_2}{dt} \qquad \Omega_1 = -\Omega \sin \theta$$

where the coordinate system is chosen so that the x_1 direction corresponds to the south-north direction and x_2 to the east-west direction. Substituting the solution (14) into (15) we have

$$\frac{d^2 u_3}{dt^2} + \omega_s{}^2 u_3 = \omega_T \Omega_1 A \cos \omega_T t$$

To the first order in ϵ there will be a component of motion along the vertical direction with a frequency ω_T. The Coriolis or gyroscopic forces tend to excite the vertical vibration with the characteristic frequency of the horizontal vibration. The amplitude of the displacement along the vertical is then

$$\omega_T \Omega_1 A / (\omega_s{}^2 - \omega_T{}^2)$$

where A is the amplitude of the oscillation in the horizontal direction.

By examining the motion of the particle in terms of a harmonic oscillator, we can reach several important conclusions about the effect of rotation on the oscillation. The rotation will cause a precession in the particle motion so that with respect to a locally fixed coordinate the direction of motion varies with time. In instruments whose response is anisotropic, there will be a variation with time of recorded amplitude because of the shift of the orientation of the particle motion with respect to the instrument. (Alsop, Sutton, and Ewing [1961b] have considered the effect of rotation on the estimation of Q of the free oscillations.) The strain-siesmometer response is a function of orientation of particle motion; detailed analysis of the decay of amplitude with time to determine Q will require consideration of the rotation of the direction of vibration. The rotation will couple horizontal motion with vertical motion so that some of the energy initially in a toroidal oscillation should appear in neighboring spheroidal oscillations, and vice versa. The amplitude of the coupled vertical motion resulting from an initial horizontal displacement depends on ϵ and on the nearness in the frequency of spheroidal and toroidal oscillations.

The expression for the change in frequency due to rotation as a function of mode number

can be obtained directly from a perturbation treatment of the equations of motion, (5) and (6). An alternative and instructive derivation applicable to both spheroidal and toroidal oscillations depends on the evaluation of the kinetic energy associated with a particular oscillation. The kinetic energy of motion relative to a coordinate system fixed in space can be written

$$K = K_R + \Omega_i h_i + \tfrac{1}{2} I_{ik} \Omega_i \Omega_k \qquad (15)$$

[*Lyttleton*, 1953], where K is the kinetic energy relative to a fixed coordinate system, K_R is the kinetic energy relative to the coordinate system rotating with angular velocity Ω_i and is

$$K_R = \tfrac{1}{2} \iiint \rho v_i v_i \, dV$$

where v_i is the velocity measured relative to the rotating coordinate system. h_i is the angular momentum relative to the rotating coordinate system

$$h_i = \iiint \rho \epsilon_{ijk} x_j v_k \, dV$$

and I_{ik} is the moment of inertia

$$I_{ij} = \iiint \rho(x_k x_k \, \delta_{ij} - x_i x_j) \, dV$$

The time-averaged kinetic energy resulting from an oscillation of frequency ω is

$$K = \iiint \rho \left\{ \frac{\omega^2}{2} \, \bar{q}_i q_i + i\omega \Omega_i \epsilon_{iks} \bar{q}_k q_s \right.$$
$$\left. + \, \Omega_i \Omega_j (\bar{q}_k q_k \, \delta_{ij} - \bar{q}_i q_j) \right\} dV \qquad (16)$$

where $\bar{q}_i$ is the complex conjugate of q_i. We now introduce the perturbation scheme described by equations 3 and 4. We note that to zero order in ϵ the moment of inertia remains constant for a toroidal oscillation. This is not the case for a spheroidal oscillation. The kinetic energy associated with the oscillation in a nonrotating system is

$$K_0 = \tfrac{1}{2}\omega_0^2 \iiint \rho \bar{q}_i^{\,0} q_i^{\,0} \, dV \qquad (17)$$

and we normalize the complex amplitudes $q_i^{\,0}$ so that

$$K_0 = \omega_0^2 \qquad (18)$$

Consider an oscillation with fixed total kinetic energy K_0. Substituting (3) and (4) into (16) and equating terms of equal order we find that the condition for the oscillation to have kinetic energy K_0 is

$$\alpha_1 = -iz_i \iiint \rho \epsilon_{iks} \bar{q}_k^{\,0} q_s^{\,0} \, dV \qquad (19)$$

The frequency ω is then the sum of the undisturbed frequency ω_0 plus the perturbation frequency ω^1.

$$\omega = \omega_0 + \omega^1$$

We note that the perturbation frequency ω^1 is determined by the part of the kinetic energy associated with the relative angular momentum (provided only that zero-order terms are kept in the expansion for the displacement q_k).

$$\omega^1 = -i\Omega_i \iiint \rho \epsilon_{iks} \bar{q}_k^{\,0} q_s^{\,0} \, dV \qquad (20)$$

Higher-order approximations may be obtained similarly.

We note that the result given in equation 20 also follows from equation 6, since q_k^0 are the eigenfunctions for the operator on the left-hand side of the equation. The condition for a solution to exist is that the scalar product of the eigenfunction q_k^0 with the right-hand side of the equation must vanish.

The expression for the first-order perturbation frequently given in equation 20 is general and applies equally well to spheroidal and toroidal oscillations. The integral in equation 19 is readily evaluated if the axis of rotation and the pole of the spherical harmonic coincide. For the toroidal oscillations we substitute the zero-order solution

$$q_k^{\,0} = [l(l+1)]^{1/2} C^m_{\,k,\,l} \, _n W_l^{\,m}(r)$$

into (19) and evaluate the integral using equation 7 and maintaining the normalization conditions expressed in equations 17 and 18. The final result is

$$\alpha_1 = m/[l(l+1)]$$

For toroidal oscillations the angular frequencies are shifted by an amount

$$\{ m/[l(l+1)] \} \Omega$$

and the degeneracy associated with the angular

order m is removed. The frequency shift is independent of n. The eigenfunctions to zero order in ϵ are normal modes of the rotating system. The displacement then takes the form

$$u_i = \sum_{l=0}^{\infty} \sum_{m=-l}^{l} \left\{ l(l+1)C^m_{i,l\,n}W_l{}^m(r) \right.$$
$$\left. \cdot \exp\left[i\left(\omega_l t + \frac{m\Omega}{l(l+1)}\right)\right]\right\} \qquad (21)$$

where ω_l is the eigenfrequency for the non-rotating system.

Equation 21 demonstrates that each value of m has two traveling waves associated with it. One wave travels eastward, and its rate of travel is decreased by the angular velocity; the other travels westward, and its rate is faster. The combined effect is to produce a standing-wave pattern that for a given value of m moves westward. The rate of advance decreases with l, the local effect being to rotate the direction of vibration of a given particle.

The magnitude of the displacement in frequency varies inversely as a square of the mode number l and is therefore greatest for the lowest mode number. For the oscillation $l = 2$ we have

$$\frac{\Omega}{l(l+1)} = 0.0069 \text{ cph} \qquad \frac{f}{\Delta f} = 206$$

The ratio of the frequency to Δf, the offset in frequency due to rotation, is 206; it is thought that the Q of the toroidal oscillations should be about 200. It therefore seems unlikely that the splitting of the toroidal oscillations can be observed unless the Q is much higher. Table 2 lists the periods for the various lines in the multiplets that would be expected in the structure of the $_0T_2$ and $_0T_3$ oscillations.

The splitting of the toroidal oscillations, unlike the splitting of the spheroidal, has not been observed. Until a detailed study of the Q for the toroidal oscillations is made it cannot be determined whether the failure to detect the splitting is due to the shortness of the record or to the fact that the Q broadens a peak by an amount greater than the distance between the rotationally separated peaks. It appears certain that there is no hope of detecting the rotational separation for any but the lowest-order toroidal oscillations.

The detailed theory of the coupling of toroidal and spheroidal oscillations has not been attempted. The qualitative considerations based

TABLE 2. Rotational Splitting of Toroidal Oscillations

Oscillations	Period, minutes	Oscillation	Period, minutes
$_0T_2{}^2$	41.9	$_0T_3{}^3$	28.43
$_0T_2{}^1$	42.1	$_0T_3{}^2$	28.48
		$_0T_3{}^1$	28.53
$_0T_2$	42.3	$_0T_3$	28.57
$_0T_2{}^{-1}$	42.5	$_0T_3{}^{-1}$	28.61
$_0T_2{}^{-2}$	42.7	$_0T_3{}^{-2}$	28.66
		$_0T_3{}^{-3}$	28.70

on harmonic oscillator models of the toroidal oscillations, however, strongly indicate the importance of this mechanism of transferring energy from one oscillation to another. It is pertinent to note that *Bogert* [1961] lists peaks in the spectrum at 28.8 minutes and 21.5 minutes which he does not identify. Bogert's observations were carried out on a long-period vertical seismometer. The listed periods are close to the observed toroidal periods for $_0T_3$ and $_0T_4$. It is possible that the unidentified peaks in Bogert's record represent the rotational conversion of initial toroidal into vertical motion. A detailed investigation of existing records of vertical instruments is indicated.

4. Core-Mantle Boundary Condition

The usual treatments of the toroidal oscillations assume as boundary conditions that the two boundaries limiting the mantle are free, spherical surfaces. The outer boundary fulfills these conditions, provided that the inhomogeneous character of the upper mantle and crust is ignored. The situation with respect to the core-mantle boundary is much less clear. Indeed, it is possible that a detailed study of the toroidal oscillations can indicate the nature of the core-mantle boundary.

High-frequency shear waves are not transmitted by the core. The agreement of the Gutenberg model earth with observations of toroidal oscillations for periods of 10 to 30 minutes (see part 6) suggests that the core behaves more or less as a fluid at these periods. The material of the core must have a certain degree of viscosity; thus the core will exert a viscous resistance to the motion of the lower boundary of the mantle. The core is composed of an electrically conducting material, and oscillations of the mantle boundary
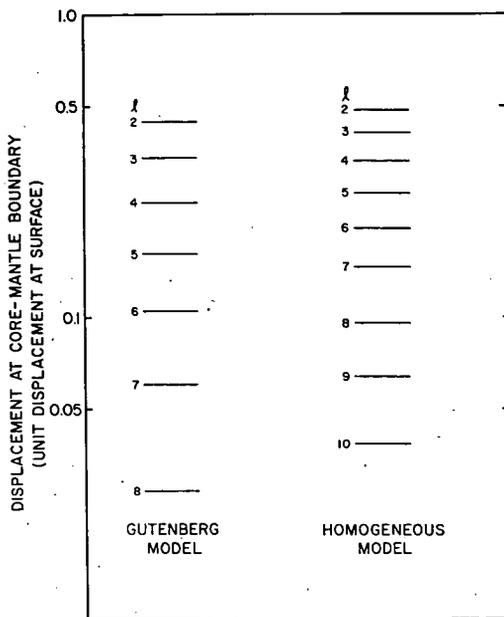
Fig. 3. Displacement at core-mantle boundary relative to unit displacement at outer surface.

TABLE 3. Estimate of Parameters at Core-Mantle Boundary

	Mantle	Core
Density ρ, g/cm³	5.7	10.6
Conductivity σ, emu	10^{-8}–10^{-9}	3×10^{-6}
Kinematic viscosity ν, cm²/sec		10^{-6} (?)
Dipole field H_r, gauss	3.8	3.8
Toroidal field H_φ, gauss	<0.1–0.01	<30
Alfvén wave velocity C_A, cm/sec	0.5	0.4
Electromagnetic viscosity η, cm²/sec	10^7–10^8	2.6×10^4

radiate magnetic energy in the form of modified Alfvén waves. Both the viscous and the hydro-magnetic interactions of the mantle and core lead to a transfer of energy from the elastic motion of the mantle into thermal and magnetic energy in the core.

The core may have some degree of elasticity, and this would lead to an apparently stiff lower boundary of the mantle. If the lower mantle is electrically conducting, the electromagnetic inter-action of the core and the mantle stiffens the boundary. In this section we investigate the quantitative effects of the dissipation of elastic energy at the core-mantle boundary, and the possible effect of the stiffness of this boundary in altering the frequencies of the toroidal oscil-lations.

The effect of the lower boundary on the oscillation is a sensitive function of the order of oscillation. In Figure 3 the displacement at the core-mantle boundary relative to a unit dis-placement at the outer surface is presented as a function of the mode number for the lower modes of oscillation for the Gutenberg model and the homogeneous model earth (see part 6). The displacement of the boundary for the Gutenberg model is less since the stiffness of this model is greater in the lower mantle than

it is in the homogeneous earth. $_0T_8$ and $_0T_2$ differ in frequency only by a factor of 4, yet the displacement at the core boundary for $_0T_8$ is 1/20 the displacement of $_0T_2$.

Table 3 lists the important parameters needed for a discussion of the core-mantle interaction. A rough measure of the importance of electro-magnetic to viscous dissipation is the ratio of the electromagnetic to the fluid viscosity η/ν. If the Bullard and Gellman [1954] estimate of the viscosity of the core is correct, electro-magnetic dissipation mechanisms outweigh the effects of viscosity. The viscosity of the core is quite uncertain, however, and if the viscosity were as high as 10^7 cm²/sec viscous effects would dominate hydromagnetic effects.

Viscous interactions of core and mantle. We first consider the effect of the viscous interaction of core and mantle independently of electro-magnetic effects. The boundary is treated as a flat plate, an approximation that is justified if the thickness of the boundary layer is small compared with the radius of the core. Table 4 lists the thickness of the boundary layer

$$\delta_r = (2\nu/\omega)^{1/2}$$

for $_0T_2$ and for various viscosities.

A viscosity of 10^4 leads to a boundary layer of only 30 meters for oscillations with a 40-minute period. For the higher modes the fre-quencies are greater and the boundary-layer thickness correspondingly less. The actual boundary-layer thickness will be substantially increased by the roughness of the surface separating the core and the mantle. Because of the small boundary-layer thickness appropriate for a smooth boundary, it is likely that irregu-

TABLE 4. Boundary-Layer Thickness for $_0T_2$

Viscosity, cm²/sec	δ_v, cm
10^{-6}	3×10^{-2}
10^{-1}	1×10^1
10^4	3×10^3
10^9	1×10^6

larities will determine the scale of the flow. Seismic methods are not capable of detecting possible 10-km irregularities.

Let the velocity of the oscillating surface be represented by

$$v = V_0 \cos \omega t$$

The stress resisting the motion at the surface is then

$$p = V_0 \rho (\omega \nu)^{1/2} \cos (\omega t + \pi/4)$$

The mean value of the energy passing through a unit area of the surface per unit time is equal to the product of the stress and velocity.

$$\overline{de/dt} = -\tfrac{1}{2} q_0^2 \omega^{5/2} \rho (\nu/2)^{1/2} \qquad (22)$$

where q_0 is the amplitude of the displacement and is a function of the angular coordinates. The total energy passing through the core-mantle boundary is then the integral of equation 22 over the surface separating the mantle from the core.

The core-mantle viscous interaction leads to a broadening of the spectral peaks as observed at the outer surface because of the energy dissipation at the boundary. The effective Q for the oscillation is determined from

$$Q = 2\pi E (dE_i'/dt)^{-1}$$

where E is the maximum elastic energy stored in an oscillation. Calculations have been carried out to evaluate Q as a function of viscosity for

an inhomogeneous Gutenberg model earth and for a homogeneous earth (see part 5). Table 5 lists these results. As can be seen, even the excessively high viscosity of 10^{14} cm²/sec leads to a high Q for the $_0T_2$ oscillation. $_0Q_6$ corresponding to a higher-frequency oscillation is greater, despite the fact that Q depends on the inverse 5/2 power of the frequency. This is because of the marked dependence of the displacement of the core boundary on the mode number. The Q for the overtone is also large, the effect of the frequency being insufficient to compensate for the lower amplitude but higher total energy in the oscillation of the overtone. The Q for the homogeneous model is lower since the displacement at the core boundary is greater in a homogeneous mantle than in the Gutenberg mantle, as was previously noted. The effective Q is large, and there will be no measurable shift in frequency resulting from the viscous interaction of core and mantle.

Electromagnetic interaction of core and mantle. The magnetic lines of force of the main dipole field intersect the core-mantle boundary at a large angle. In the toroidal mode of oscillation the mantle moves parallel to the core-mantle boundary, and this motion induces an electromotive force perpendicular to the dipole field and thus approximately parallel to the core-mantle boundary. The electric field produces currents which flow both in the core and in the lower mantle.

The coupling of the electromagnetic field and the velocity field in the core fluid results in a disturbance in the material motion at and near the boundary surface. The disturbance will be propagated as Alfvén waves along the lines of force that intersect the boundary. The Alfvén waves are damped because of the viscosity and the finite electrical conductivity of the core fluid. Eddy currents dissipate energy both in the core and mantle.

TABLE 5. Effective Q of Oscillation Due to Viscous Interaction of Core and Mantle

Viscosity, cm /sec	Q for $_0T_2$		Q for $_0T_6$		Q for $_1T_2$	
	Homogeneous Earth	Gutenberg Model Earth	Homogeneous Earth	Gutenberg Model Earth	Homogeneous Earth	Gutenberg Model Earth
10^{14}	8.8×10^3	9.1×10^3	9.0×10^3	1.3×10^4	5.7×10^2	8.6×10^2
10^4	8.8×10^8	9.1×10^8	9.0×10^8	1.3×10^8	5.7×10^7	8.6×10^7
10^{-6}	8.8×10^{13}	9.1×10^{13}	9.0×10^{13}	1.3×10^{14}	5.7×10^{12}	8.6×10^{12}

Electromagnetic Viscosity, cm²/sec		δ for $_0T_2$, km	δ for $_0T_6$, km
Mantle	10^7	0.9	0.5
	10^8	2.8	1.6
Core	2.6×10^4	0.05	0.03

The total stress acting on the boundary surface is due to two components. One is the viscous stress perturbed by the presence of the electromagnetic field, and the second is a Maxwell stress due to the component of the magnetic field parallel to the core-mantle boundary. In the following paragraphs, we will evaluate the magnitude of the Maxwell stress acting on the oscillating surface and the perturbation of the flow field in the core due to electromagnetic effects.

The hydromagnetic theory of the origin of the earth's magnetic field requires the presence of a toroidal field within the core. Because of the finite conductivity of the lower mantle, the permanent toroidal field leaks into the lower mantle. The toroidal field within the lower part of the mantle combined with the dipole field exerts a steady Maxwell stress on the lower boundary. The magnitude of the stress depends on the strength of the toroidal field in the upper part of the core and on the conductivity of the lower mantle. *Rikitake* [1955] has estimated that a toroidal field as high as 30 gauss may exist in the upper core. The conductivity of the lower mantle has been estimated by *Tozer* [1960] to be 10^{-9} emu, although H. Hughes has suggested a somewhat greater conductivity at this depth on the basis of the theory of electrical conductivity in solids at high temperatures. The indicated Maxwell stress is 0.03 to 0.003 dyne/cm². Alfvén waves will not be excited along the toroidal lines of force, since they do not intersect the core-mantle boundary. As a first approximation we suppose that the steady Maxwell stress exerted by the combined toroidal dipole field on the lower mantle boundary does not affect the oscillatory motion of the surface. Later in this section we will consider the effects of the steady Maxwell stress on the frequencies of the toroidal oscillations.

The core-mantle boundary will again be treated as a smooth plane. The justification of the plane approximation requires that the skin depth of the disturbances in the mantle and the magnetohydrodynamic boundary layer thickness be small compared with the radius of the core. Table 6 lists representative values for the electromagnetic skin depth δ, where

$$\delta = (2\eta/\omega)^{1/2} = \sqrt{1/2\pi\omega\mu\sigma}$$

with the electromagnetic viscosity $\eta = 1/4\pi\mu\sigma$ (see Table 3).

Electromagnetic units will be used in the following discussion. The permeability μ is assumed to be unity, since it is improbable that there are ferromagnetic materials at the temperatures that must exist at those depths. The skin depths and boundary-layer thicknesses are much smaller than the dimensions of the core. This also suggests that there is no need to consider reflection from other boundaries. The question of the effect of surface roughness, however, remains open.

The problem of the motion of a flat plate in the presence of a magnetic field has been considered by a number of workers. *Ludford* [1959] studied the problem of the impulsive motion of a flat plate, assuming an infinite conductivity for the material of the plate. *Kakutani* [1958] and *Hide and Roberts* [1960] have discussed the motion of an insulator, and these solutions are contained implicitly in the work of *Lin* [1958], who generalized many of the exact solutions of fluid dynamics to problems of hydromagnetics. The case of a plate of finite conductivity has not been treated.

The geometry adopted is shown in Figure 4, the steady magnetic field being perpendicular to the boundary between the fluid and solid. As a result of the motion, the perturbation field is set up parallel to the boundary with the current perpendicular to the plane defined by the velocity vector and the magnetic field. Let H_i, v_i, and j_i represent the magnetic field
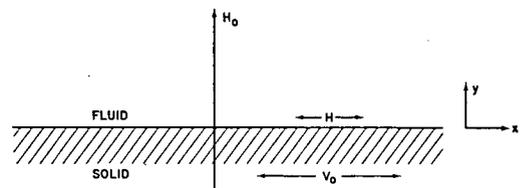
Fig. 4. Geometry for the oscillating plate problem.

intensity, velocity, and current density, respectively.

$$H_i = (H_1, H_2, 0)$$

$$v_i = (v_1, 0, 0)$$

$$j_i = (0, 0, j_3)$$

The fluid is taken to be incompressible

$$\partial v_i / \partial x_i = 0$$

The equation of motion in the absence of rotation and neglecting gravity is

$$\rho \frac{dv_i}{dt} = \mu \epsilon_{imn} j_m H_n - \frac{\partial p}{\partial x_i} \quad (23)$$

and Ohm's law is given by

$$j_m = \sigma(E_m + \mu \epsilon_{mns} v_n H_s)$$

where p represents the pressure and E the electric field intensity. Under the standard approximation of magnetohydrodynamics [*Cowling*, 1957], Maxwell's equations combine as follows:

$$\frac{\partial H_i}{\partial t} = H_i \frac{\partial V_i}{\partial x_i} - v_i \frac{\partial H_i}{\partial x_i} + \eta \frac{\partial^2 H_i}{\partial x_k \partial x_k} \quad (24)$$

Let $H_2 = H_0 + H_2{}^1$, and assume that there is no x_1 dependence of the magnetic, velocity, and pressure fields. Then (23) and (24) yield

$$\frac{\partial H_1}{\partial t} = \eta \frac{\partial^2 H_1}{\partial y^2} + v_1 \frac{\partial H_2{}^1}{\partial y}$$
$$+ (H_0 + H_2{}^1) \frac{\partial V_1}{\partial y} \quad (25)$$

$$\frac{\partial H_2{}^1}{\partial t} = \eta \frac{\partial^2 H_2{}^1}{\partial y^2} \quad (26)$$

$$\frac{\partial v_1}{\partial t} = \nu \frac{\partial^2 v_1}{\partial y^2} + \frac{\mu(H_0 + H_2{}^1)}{4\pi\rho} \frac{\partial H_1}{\partial y} \quad (27)$$

$$\frac{\partial p}{\partial y} = -\frac{\mu H_1}{4\pi} \frac{\partial H_1}{\partial y} = -\frac{1}{2} \frac{\partial}{\partial y}\left(\frac{\mu H_1{}^2}{4\pi}\right) \quad (28)$$

Equation 28 can be integrated directly to yield $p = -\mu H_1{}^2/8\pi$, giving the tensional forces involved in Alfvén wave propagation. We can decouple (26) from (25) and (27) by assuming that $|H_2{}^1/H_0| \ll 1$, which supposes that the perturbation field in the direction of the main field is relatively small. Let C_A represent the Alfvén wave velocity, $C_A{}^2 = \mu H_0{}^3/4\pi\rho$. Then

(25) and (27) become

$$\frac{\partial H}{\partial t} = \eta \frac{\partial^2 H}{\partial y^2} + H_0 \frac{\partial v}{\partial y} \quad (29)$$

$$\frac{\partial v}{\partial t} = \nu \frac{\partial^2 v_1}{\partial y^2} + \left(\frac{C_A{}^2}{H_0}\right) \frac{\partial H}{\partial y} \quad (30)$$

where for clarity H_i has been expressed as $H_i = (H, H_0, 0)$.

The boundary condition at the solid-fluid interface is that the velocity of the viscous fluid is equal to the velocity of the plate. The plate velocity is

$$v = V_0 e^{i\omega t} \quad (31)$$

so that

$$v = V_0 e^{i\omega t}|_{y=0}$$

The boundary conditions on the normal and tangential components of the magnetic field are

$$H_2|_s = H_2|_f \quad (32)$$

$$H_1|_s = H_1|_f \quad (33)$$

where the subscripts s and f denote the solid and fluid components. Equation 32 is satisfied automatically by our approximation that

$$|H_2{}^1/H_0| \ll 1$$

Finally there is the condition on the tangential component of the electric field being continuous at the core-mantle boundary. The continuity of the normal component of the magnetic induction requires

$$\frac{1}{\sigma} \frac{\partial H_1}{\partial y}\bigg|_f = \frac{1}{\sigma} \frac{\partial H_1}{\partial y}\bigg|_s \quad (34)$$

The elasticity of the plate is neglected, since the stress gradients across the skin depth are small. Equation 29 takes the form

$$\frac{\partial H}{\partial t} = \eta \frac{\partial^2 H}{\partial y^2} \quad (35)$$

in the solid. The appropriate solution to the diffusion equation 35 is

$$H = D \exp\left[\frac{y}{\delta_s} + i\left(\omega t + \frac{y}{\delta_s}\right)\right]$$

where D is a constant coefficient to be determined from the boundary conditions. This solution is chosen to give a vanishing perturbation field, H, at large negative values of the coordinate y.

The solution for the velocity field is taken in the form [*Ludford*, 1959]

$$v = [Ae^{-k_1 y} + Be^{-k_2 y}]e^{i\omega t} \qquad (36)$$

A and B are constants determined by the boundary conditions, and k_1 and k_2 are determined from (29) and (30). The perturbation field in the fluid is then

$$H = \frac{H_0}{C_A^2}\left[\frac{A}{k_1} e^{-k_1 y}(k_1^2 \nu - i\omega)\right.$$

$$\left. + \frac{B}{k_2} e^{-k_2 y}(k_2^2 \nu - i\omega)\right]$$

The solution has been chosen so that the velocity field vanishes at large positive values of the coordinate y. Ludford has shown that the dispersion relations give

$$k_1 = \frac{1}{2(\eta\nu)^{1/2}}\{[C_A^2 + i(\eta^{1/2} + \nu^{1/2})^2\omega]^{1/2}$$

$$+ [C_A^2 + i(\eta^{1/2} - \nu^{1/2})^2\omega]^{1/2}\} \qquad (37)$$

$$k_2 = \frac{1}{2(\eta\nu)^{1/2}}\{[C_A^2 + i(\eta^{1/2} + \nu)^2\omega]^{1/2}$$

$$- [C_A^2 + i(\eta - \nu^{1/2})^2\omega]^{1/2}\} \qquad (38)$$

In the limit of low frequency, the disturbance is an Alfvén wave propagated with a perturbed Alfvén wave velocity. The perturbations result from the finite viscosity and conductivity of the fluid.

The contributions of the energy radiated from the plate as Alfvén waves and of that going into dissipation by viscosity and conductivity near the boundary are given by the ratio of the two terms in each of the square brackets of equations 37 and 38. It is convenient to separate the effects of conductivity and viscosity by the introduction of the dimensionless quantities

$$\alpha = C_A^2/\omega\eta_f \qquad \beta = (\nu/\eta_f)^{1/2}$$

α is a measure of the ratio of energy radiated away to that lost by dissipation due to the finite conductivity of the fluid. β is a measure of the ratio of dissipation due to viscous effects relative to that due to the finite electrical conductivity of the fluid. In terms of the constants α and β, the mode numbers k_1 and k_2 are given by

TABLE 7.   Dimensionless Parameters at Core-Mantle Boundary

$\alpha = 2.5 \times 10^{-3}$			
$\beta =$	$\nu = 10^{-6}$	10^4	10^{14}
	6×10^{-6}	0.6	6×10^4
$\gamma = 0.02-0.05$			

$$k_1 = \frac{1}{\sqrt{2\beta\,\delta_f}}\{[\alpha + i(1 + \beta)^2]^{1/2}$$

$$+ [\alpha + i(1 - \beta)^2]^{1/2}\}$$

$$k_2 = \frac{1}{\sqrt{2\beta\,\delta_f}}\{[\alpha + 1(1 + \beta)^2]^{1/2}$$

$$- [\alpha + i(1 - \beta)^2]^{1/2}\}$$

A parameter useful in discussing the relative contributions of eddy-current dissipation in the solid and fluid is

$$\gamma = \delta_f/\delta_s = (\sigma_s/\sigma_f)^{1/2}$$

Representative values of the dimensionless parameters α, β, and γ are listed in Table 7. α is the best known of these parameters. *Bullard and Gellman* [1954] adopt a value for the conductivity of the core of 3×10^{-6} emu and state that this value is uncertain by no more than 30 per cent. Several other estimates of the conductivity based on the extrapolation of near-surface values lead to much the same value, though studies of the westward drift of the field suggest a conductivity lower by an order of magnitude. If anything, the value adopted by Bullard for the conductivity of the core is too high. A lower value would lead to a correspondingly lower value for α. The value for β is uncertain because of the inconclusive evidence concerning the value of the viscosity for the core. *Jeffreys* [1952] has attempted an estimate on the basis of the damping of P waves in the core. Aside from difficulties in interpretation of the seismic results this will give an estimate of the bulk viscosity rather than the shear viscosity, which is of interest for the boundary-layer problem. *Gutenberg* [1959a] considers the problem of viscosity of the core completely open.

The stress resisting the oscillation of the solid surface will be composed of a viscous plus a Maxwell stress.

$$p_{12} = \rho\nu\left.\frac{\partial v}{\partial y}\right|_{v=0} + \left.\frac{H_0 H}{4\pi}\right|_{v=0}$$

In terms of the solution (36), the gradient of the fluid velocity is

$$\frac{\partial v}{\partial y}\bigg|_{v=0} = -(k_1 A + k_2 B)e^{i\omega t}$$

which combined with the boundary condition on the velocity

$$v = V_0 e^{i\omega t} \quad \text{at} \quad y = 0$$

yields

$$\frac{\partial v}{\partial y}\bigg|_{v=0} = [A(k_2 - k_1) - k_2 V_0]e^{i\omega t}$$

The perturbation field H at the boundary $y = 0$ in the solid is

$$H|_{v=0} = De^{i\omega t}$$

The total stress acting on the plate in terms of the mode numbers and undetermined constants is then

$$p_{12} = \left\{\rho\nu\left[A(k_2 - k_1) - k_2 V_0 + \frac{DH_0}{4\pi}\right]\right\}e^{i\omega t}$$

The average energy dissipated at the boundary is

$$\frac{\overline{de}}{dt} = -\frac{\rho\nu}{2}\, V_0\left[A(k_2 - k_1) - k_2 V_0 + \frac{DH_0}{4\pi\,\rho\nu}\right]$$

The boundary conditions in equations 31, 33, and 34 provide the three equations for determining the three constants A, B, and D, which are, respectively

$$A + B = V_0$$

$$\frac{H_0}{C_A{}^2}[A(i\omega - k_1{}^2\nu) + B(i\omega - k_2\nu)] = D$$

and

$$\frac{1}{\sigma_f}\frac{H_0}{C_A{}^2}[A(i\omega - k_1{}^2\nu) + B(i\omega - k_2{}^2\nu)]$$

$$= \frac{D}{\sigma_s}\cdot\frac{(1 + i)}{\delta_s}$$

The solution for D is found to be

$$D = \frac{- V_0\sqrt{2}\gamma H_0{}^2(\eta_f\nu)^{1/2}}{(1 + i)(1 + \beta) + \sqrt{2}[\alpha + i(1 + \beta)^2]^{1/2}\gamma}$$

Solving for A and B in terms of the dimensionless parameters, we find that the rate of energy dissipated per unit area of the surface is given exactly by

$$\frac{\overline{de}}{dt} = \frac{-\rho\nu V_0{}^2}{2[\alpha + i(1 + \beta)^2]^{1/2}}\left(\frac{\omega}{\nu}\right)^{1/2}\bigg\{i(1 + \beta)$$

$$+ \frac{\alpha(1 + i)}{(1 + i)(1 + \beta) + \sqrt{2}\gamma[\alpha + i(1 + \beta)^2]^{1/2}}$$

$$+ \sqrt{2}\left(\frac{\alpha}{\beta}\right)(1 + i)(1 + \beta)$$

$$+ \sqrt{2}[\alpha + i(1 + \beta)^2]^{1/2}\bigg\} \tag{39}$$

The term in the braces represents the modified viscous dissipation; the second term describes the eddy-current dissipation in the fluid; the third term is due to the dissipation by eddy currents in the solid as represented by the Maxwell stress. The terms involving γ arise from the finite conductivity of the solid, and those involving α are associated with the magnetohydrodynamic modes.

The parameter α is small because of the relatively small dipole field of the core-mantle boundary. As a result, the magnetohydrodynamic effect will be important only when β is small. For the case of small viscosity for the core $\beta \ll 1$, the average energy flux is

$$\frac{\overline{de}}{dt} = \frac{-\rho\nu^{1/2}\omega^{1/2}}{2\sqrt{2}}\left\{1 + \frac{\alpha}{\beta}\frac{\gamma}{1 + \gamma}\right\}V_0{}^2 \quad \begin{cases}\alpha \ll 1 \\ \beta \ll 1\end{cases}$$

The dissipation due to the finite conductivity of the mantle dominates the viscous dissipation when

$$\frac{\alpha\gamma}{\beta} \gg 1 \qquad \left(\frac{\mu}{4\pi}\right)^{1/2}\frac{H_0{}^2\sigma_s}{\rho\omega\sqrt{\nu}} \gg 1$$

Eddy-current dissipation is thus favored by low-frequency oscillations and high conductivity of the mantle.

In terms of the displacement q_0 of the plate the eddy-current dissipation is

$$\frac{\overline{de}}{dt} = -\frac{\rho C_A{}^2\omega^{3/2}}{4\eta_f{}^{1/2}}\frac{\sigma_s}{\sigma_f + \sigma_s}\, q_0{}^2$$

The eddy-current dissipation depends on the 3/2 power of the frequency; ordinary viscous dissipation, on the 5/2 power of the frequency.

The relative contribution of the eddy-current dissipation to the viscous dissipation is shown in Figure 5, in which the ratio of the Maxwell stress to the viscous stress is presented as a function of the conductivity of the lower mantle
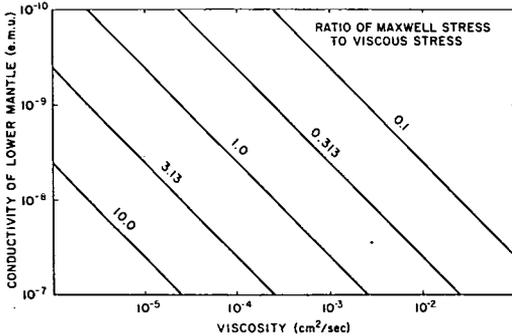
Fig. 5. Ratio of energy dissipated by eddy currents to that dissipated by viscosity.

TABLE 8. Values of λ_{eff} for the Gutenberg and Homogeneous Model Earth
$\lambda_{eff} = (\omega^2_{stiff} - \omega^2_{free})/\omega^2_{free}$

Oscillation	λ_{eff} Homogeneous	λ_{eff} Gutenberg
$_0T_2$	0.58	0.84
$_0T_3$	0.19	0.25
$_0T_4$	0.08	0.06
$_0T_6$	0.018	0.016
$_0T_{10}$	0.001	0.000
$_1T_2$	0.64	0.57

and the viscosity of the core. If the viscosity of the core is 10^{-3} cm²/sec, the eddy current contributes as much to the dissipation as the viscous stress does, provided that the conductivity of the lower mantle is 2.5×10^{-7} emu. These considerations indicate that for probable values of the core viscosity and the core-mantle conductivity (see Table 3) the viscous dissipation greatly exceeds the hydromagnetic dissipation at the frequencies of the toroidal oscillations. In motions of lower frequencies, however, such as the Chandler wobble, the electromagnetic dissipation should dominate.

As β approaches unity, and becomes large, the expression for the average rate of energy dissipation (equation 39) approaches the energy dissipated by pure viscosity, and we obtain the results discussed in the previous section.

Effect of the steady toroidal magnetic field on the lower boundary of the mantle. The toroidal field in the core leaks into the mantle because of the finite conductivity of the mantle. The pondermotive force exerted by the field on the mantle is

$$\frac{1}{4\pi} \left\{ \left(\frac{H_\theta}{r} \sin \theta \right) \frac{\partial}{\partial \theta} (\sin \theta H_\varphi) \right.$$

$$\left. + \left(\frac{H_r}{r} \right) \frac{\partial}{\partial r} (rH_\varphi) \right\}$$

H_r, the radial component of the magnetic field, is approximately equal to the dipole field. H_φ is the toroidal component of the field in the lower mantle. The conductivity of the lower mantle is presumed to decrease outward in a radial direction, and therefore the toroidal field is confined to a thin spherical shell near the core-mantle boundary. The pondermotive force is, to this degree of approximation,

$$(H_r/4\pi)(\partial H_\varphi/\partial r) \qquad (40)$$

The total force, acting on the mantle, follows from integrating equation 40 over the mantle. We neglect radial variations in the dipole field; the stress acting on the mantle is $H_r H_\varphi/4\pi$. This stress couples the mantle to the core and, indeed, is supposed to be responsible for transmitting variable core motions to the mantle with a resulting variation in length of day [*Munk and MacDonald*, 1960].

The magnitude of the Maxwell stress depends on the strength of the toroidal field in the core and on the conductivity of the lower mantle. Pertinent estimates are listed in Table 3. The stresses corresponding to the listed values of the toroidal field are 0.03 to 0.003 dynes/cm².

Suppose that the lower boundary of the mantle is kept rigid. The stress at the core-mantle boundary required to maintain a rigid boundary varies as

$$\tau(b) = \tau_0(b) \cos \omega t$$

where ω is the frequency of the oscillation and $\tau_0(b)$ is the maximum stress. Direct calculation shows that, for the Gutenberg model, the maximum stress is

$$\tau_0(b) = 1.5 \times 10^4 q_0(a) \quad \text{dynes/cm}^2$$

where $q_0(a)$ is the maximum outer surface displacement (see parts 5 and 6). If for a given surface displacement $q_0(a)$, $\tau_0(b)$ is less than the Maxwell stress, the surface is rigid throughout the oscillation and the frequency of the oscillation will be higher than in the case of a free boundary. Table 8 lists the proportional increase in the frequency for various oscillations. If the stress generated at the core-mantle boundary is greater than the critical Maxwell stress τ_M, then
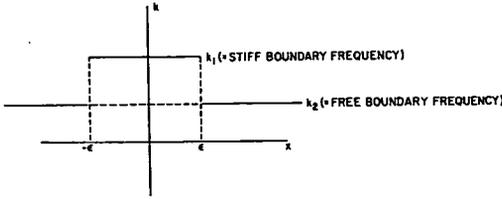
Fig. 6. Amplitude-dependent spring constant.

over part of the oscillation the boundary acts as if it were rigid. The situation is analogous to the case of solid friction. A force below a certain critical value does not move a block resting on a solid but will result only in the elastic deformation of the block. Forces in excess of this critical force move the block over the resisting surface with a sliding friction less than the static friction.

In the following, we obtain an approximate expression for the shift in frequency for oscillations with a partly rigid boundary. Each oscillation is modeled by a spring-mass system with a variable spring constant. For stresses below some critical stress determined by the toroidal field and conductivity in the lower mantle, the lower boundary acts as a stiff boundary; above this critical stress the boundary is free. The variable spring constant is schematically illustrated in Figure 6, where ϵ is the displacement corresponding to the critical Maxwell stress. In the lumped constant approximation for the toroidal oscillation, k_1 is the larger spring constant corresponding to the high-frequency, stiff lower boundary oscillation ω_1, and k_2 represents the low-frequency, free lower boundary oscillation ω_2. The equation for the lumped constant harmonic oscillator is then

$$d^2x/dt^2 + k_2x$$
$$= -\lambda k_2[H(x + \epsilon) - H(x - \epsilon)] \quad (41)$$
$$\lambda = (\omega_1{}^2 - \omega_2{}^2)/\omega_2{}^2$$

where $H(x)$ is a unit step function and dissipation both in the mantle and at the boundary has been neglected. Table 8 lists values for the effective λ for certain oscillations of the Gutenberg and the homogeneous models. In the analogy with the nonlinear spring-mass system, the frequencies of oscillation have been determined from actual model computations for a stiff and a free core-mantle boundary (see part 6). Table 8 again illustrates the fact that the low-order modes are

far more dependent on the lower boundary condition than the high-order modes.

The period of the nonlinear harmonic oscillators described by equation 41 can be obtained either by the method of Krylov-Bogoliuboff [Minorsky, 1957] or by direct integration of the energy equation. The latter procedure leads to the exact expression for the period T.

$$T = 4\left\{ \frac{1}{[k_2(1 + \lambda)]^{1/2}} \sin^{-1}\left[\left(\epsilon\sqrt{\frac{1 + \lambda}{x_m{}^2 + \lambda\epsilon^2}}\right)\right] + \frac{1}{k_2{}^{1/2}} - \frac{1}{\sqrt{k_2}} \sin^{-1}\left[\frac{\epsilon}{x_m}\right]\right\}$$

x_m is the maximum amplitude of the oscillation. Let T_0 represent the period for the oscillation if the lower boundary is free ($k_1 = k_2$). The perturbed period T is then given approximately by

$$T/T_0 = 1 - \tfrac{1}{3}(\epsilon/x_m)^3\lambda$$

with the condition for the validity of the approximation

$$\lambda(\epsilon/x_m)^2 \ll 1$$

The ratio ϵ/x_m is the proportion of the amplitude over which the harmonic oscillator reacts to the stiffer spring. This implies for the toroidal oscillations that a partly rigid boundary will affect the period of the oscillation only if $\tau_0(b)$ is of the same magnitude as the critical Maxwell stress. The Maxwell stress tying the core with the mantle is of the order of 0.03 to 0.003 dyne/cm^2, provided that the estimates of the magnetic field and conductivity are correct.

The analysis by Benioff, Press, and Smith [1961] shows a peak of the toroidal oscillations at a period of 42.3 minutes (see part 1). Benioff, Harrison, LaCoste, Munk, and Slichter [1959] determined the noise level for the Benioff extensometer at Isabella, finding that the root mean square error in strain is very nearly the least count of about 1×10^{-10}. The extensometer is 24.08 meters long, so that the minimum measurable displacement is about 10^{-7} cm. The records for the Chilean earthquake of both of the Nana and Isabella extensometers all indicate readings well above the noise level, suggesting a maximum surface displacement of at least 10^{-6} cm. For a surface displacement of this magnitude the corresponding stress at the core-mantle boundary needed to maintain a rigid boundary is 0.01 dyne/cm^2. This stress is of
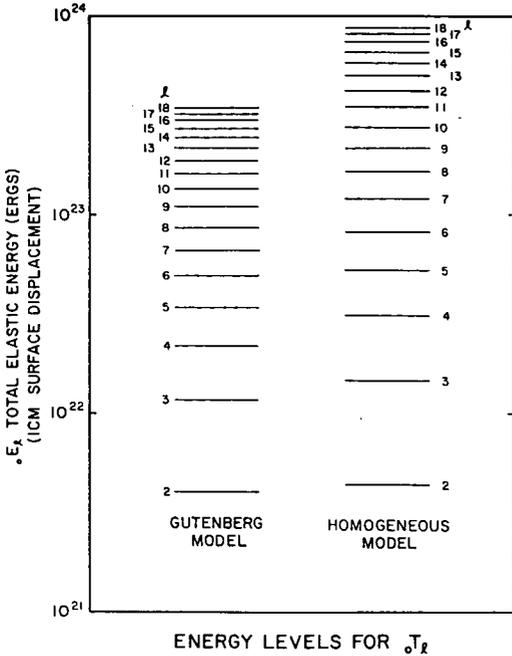
Fig. 7. Total elastic energy in $_0T_l$.

the same order as the computed electromagnetic stress. The observed frequency $_0T_2$ is somewhat greater than that expected for a Gutenberg model free boundary (see part 6) but much less than the stiff boundary. It should be noted that, if the electromagnetic stress is actually 0.3 dyne/cm², corresponding to a high mantle conductivity and toroidal field, the mantle should act with a stiff lower boundary.

The data on the $_0T_2$ oscillations are not sufficiently precise to allow a definite statement on the extent of the core-mantle interaction. If the ratio of the perturbed period to the free period is taken as 42.3/43.6, the critical Maxwell stress is

$$\tau_0(b)\left[\frac{3}{\lambda}\left(1 - \frac{T}{T_0}\right)\right]^{1/3}$$

or

$$(1.5 \times 10^4)(10^{-6})\left[\frac{3}{0.84}\left(1 - \frac{42.3}{43.6}\right)\right]^{1/3}$$

$$\cong 7 \times 10^{-3} \quad \text{dyne/cm}^2$$

Thus it appears that the electromagnetic stress could be of sufficient magnitude to perturb the mantle oscillations. The effect of the magnetic

stiffness would be to increase the frequency of the oscillations. The observed $_0T_2$ oscillation is close to the value predicted for the Gutenberg model with a free lower boundary, so that the toroidal magnetic field in the lower mantle has a strength less than about 0.1 gauss. This requires that the toroidal field in the core is lower than 10 gauss if the conductivity of the lower mantle is 10^{-8}. It is even lower if the mantle conductivity is higher.

We further note that because of dissipative processes within the mantle and at the boundary the amplitude of the $_0T_2$ oscillation at the core-mantle boundary will decrease with time. As the amplitude decreases the perturbations due to the finite boundary stress increase, and there should be a corresponding shift in frequency. Analysis of the frequency of the $_0T_2$ oscillations as a function of time should indicate a shift in frequency. We have attempted such a study of the Lamont record, but the record is too short to give definitive results.

The $_0T_2$ oscillation should show the effects of the steady electromagnetic coupling for the core-mantle to a greater extent than the other oscillations. This is apparent both from the tabulations of the parameter λ in Table 8 and from the
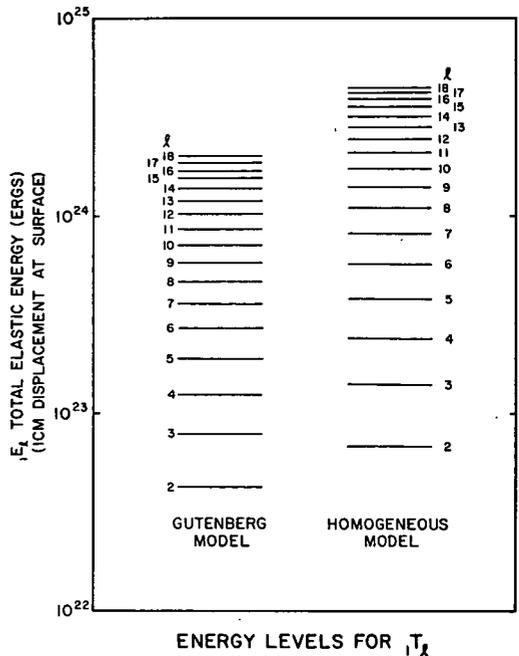
Fig. 8. Total elastic energy in $_1T_l$.
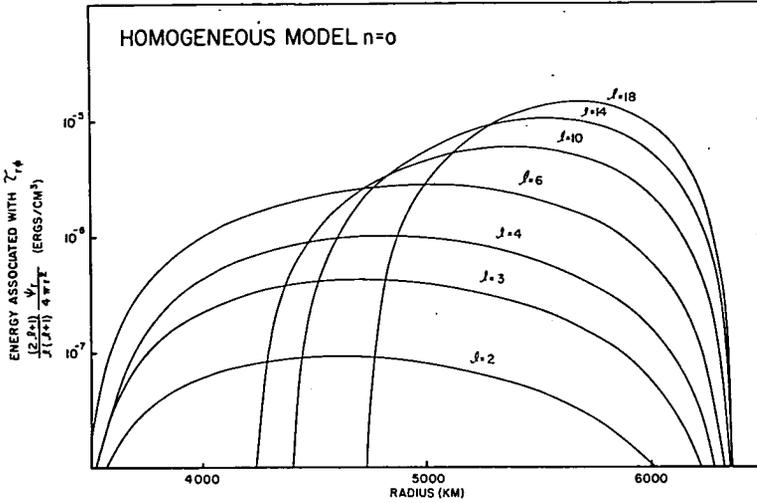
Fig. 9. Elastic energy per volume associated with radial stress in a homogeneous mantle $(_0T_l)$.

fact that higher-order oscillations require a greater stress in order to maintain a rigid lower boundary.

The placing of a requirement on the magnitude of the toroidal field in the lower mantle provides further difficulties for the interpretation of the irregularities of the rotation of the earth, in terms of the core-mantle interaction. *Munk and MacDonald* [1960] have discussed these irregularities. They find that a toroidal field in the mantle of about 0.1 gauss is required to account for the longer-period irregularities in rotation by core-mantle interaction. The above interpretation for the $_0T_2$ toroidal oscillations suggests that the toroidal field is less than this.

5. DISTRIBUTION OF ENERGY

In the present section we neglect the effects of dissipation and rotation and consider the equation of motion to zero order in ϵ. In a toroidal oscillation there is an equal partition between kinetic and elastic energy over one or more cycles of oscillation. The radial distribution of elastic energy is a function of the mode number.
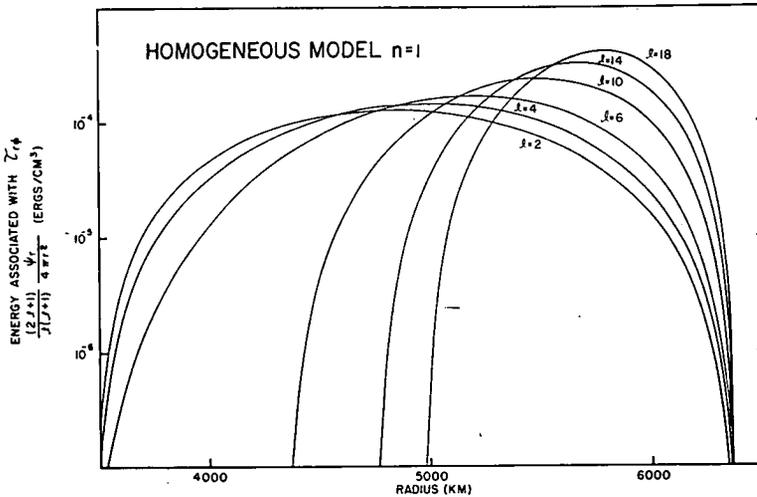
Fig. 10. Elastic energy per unit volume associated with radial stress in a homogeneous mantle $(_1T_l)$.
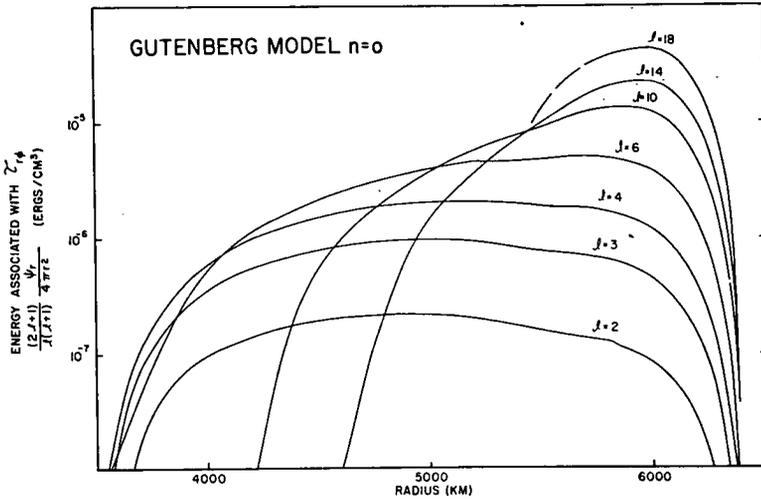
Fig. 11. Elastic energy per unit volume associated with radial stress for Gutenberg model earth ($_0T_l$).

In any given mode of oscillation the mean elastic energy will be a function of radius, depending on the distribution of elastic constants. A knowledge of the radial variation of elastic energy with mode number is essential in the construction of different models of the earth. A given model is defined by the distribution of shear-wave velocity C_S and rigidity μ. Any discrepancy between the theoretically computed and the observed resonant frequencies can be assigned to incorrect values of the elastic parameters. For a given mode, certain regions of the earth are more disturbed by the oscillation than others, and the corresponding rigidities and velocities play a greater role in determining the resonant frequency. Distribution of energy fixes the regions of the earth that contribute most heavily in determining a particular resonant frequency.

The radial distribution of energy for a given mode is also essential to the interpretation of the values of Q obtained from observations. Different modes will effectively sample different parts of the earth's mantle; the Q's obtained for the
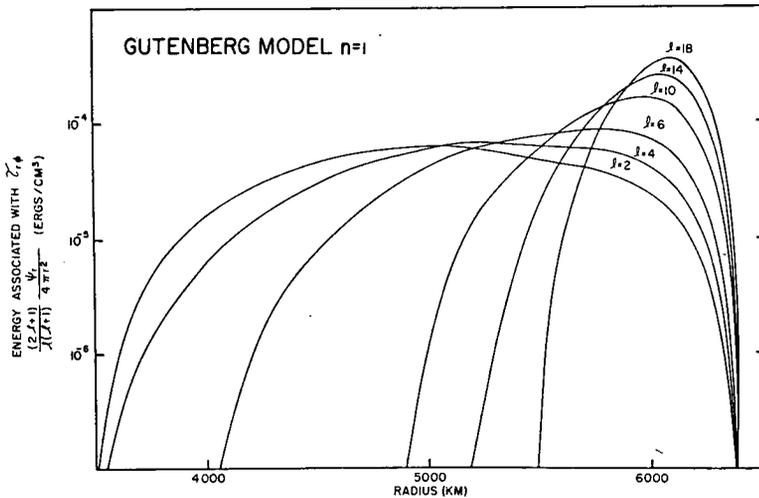
Fig. 12. Elastic energy per unit volume associated with radial stress for Gutenberg model earth ($_1T_l$).
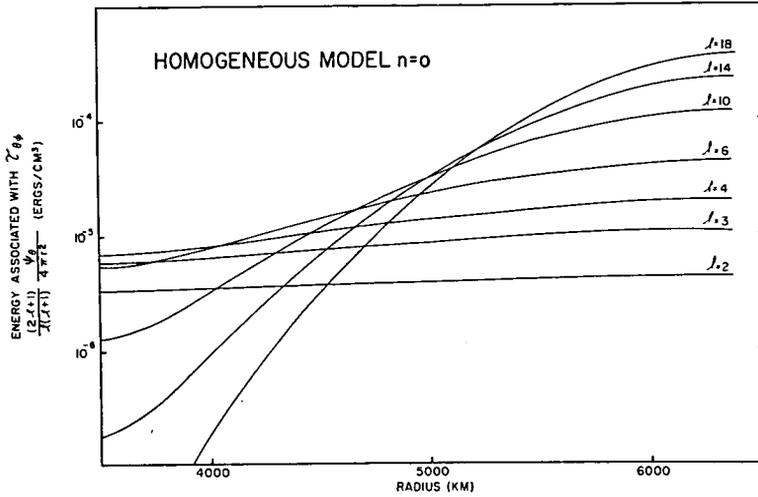
Fig. 13.   Elastic energy per unit volume associated with conical stress for homogeneous earth $(_0 T_l)$.

different modes allow an estimate of the radial variation of the dissipative properties.

The variation with mode number of the total energy in a mode of oscillation is useful in the determination of the energy spectrum of an earthquake. The surface displacement at a given frequency at a point on the earth's surface specifies the total elastic energy in that mode of oscillation. It thus may be possible to calibrate the intensity of large earthquakes exciting the free oscillations in terms of the energies within specific modes of oscillation.

The mode number m is set equal to zero since, in a nonrotating body, the modes are degenerate with respect to m. The neglect of rotational effects in the energy consideration implies that we neglect terms of order ϵ^2. For $m = 0$ the surface displacement corresponding to an oscillation of a given order l is

$$_n q_{r,l} = 0 \qquad _n q_{\theta,l} = 0$$

$$_n q_{\varphi,l} = P_l^{1}(\cos \theta) \, _n W_l(a) \qquad (42)$$

where a is the outer radius. The computed
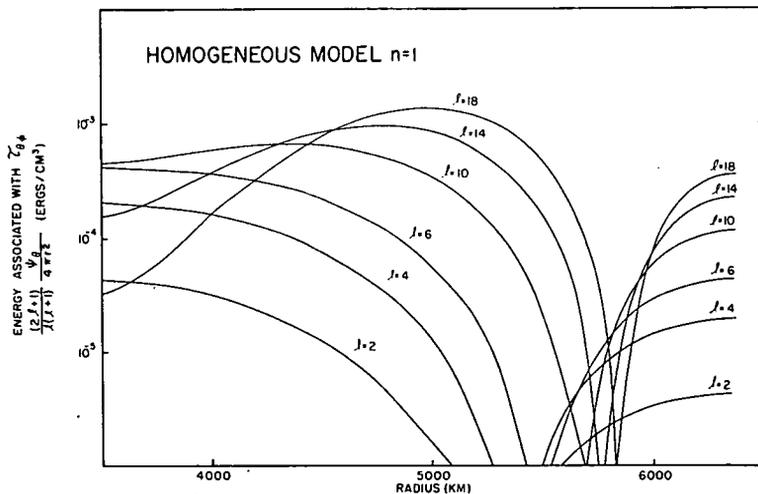
Fig. 14.   Elastic energy per unit volume associated with conical stress for homogeneous earth $(_1 T_l)$.
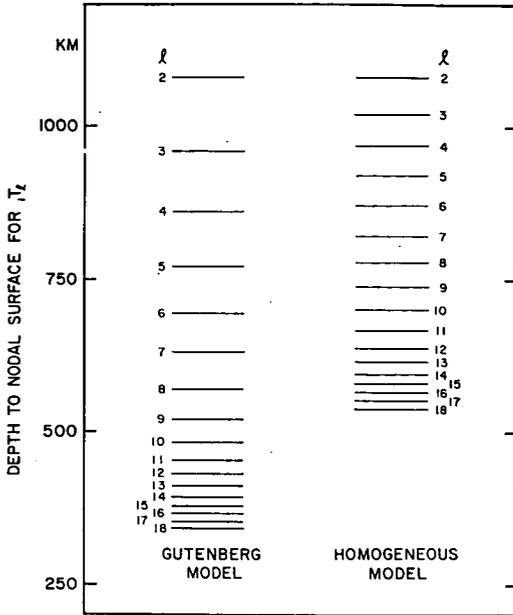
Fig. 15. Depth to nodal surface in homogeneous and Gutenberg model earth.

energies are normalized such that

$$_n q_{\varphi,l}(a) = P_l{}^1 (\cos \theta) \qquad (43)$$

and the radial function $_n W_l$ is set equal to 1 cm at the outer surface. The surface distribution of displacement for the first few orders is then

$$_n q_{\varphi,2}(a) = \tfrac{3}{2} \sin 2\theta$$

$$_n q_{\varphi,3}(a) = \tfrac{3}{8}(\sin \theta + 5 \sin 3\theta)$$

$$_n q_{\varphi,4}(a) = \tfrac{5}{16}(2 \sin 2\theta + 7 \sin 4\theta)$$

where the pole of the harmonic is fixed by the source of the disturbance, and θ is the angle between the source and receiver, not the geographical colatitude.

The nonvanishing components of the strain are

$$\epsilon_{r\varphi} = \frac{1}{2} \left(\frac{\partial q_\varphi}{\partial r} - \frac{q_\varphi}{r} \right)$$

$$\epsilon_{\theta\varphi} = \frac{1}{2} \left(\frac{1}{r} \frac{\partial q_\varphi}{\partial \theta} - \cot \theta \, \frac{q_\varphi}{r} \right)$$

for the displacement given by equation 42. The corresponding nonvanishing components of the stress are

$$\tau_{r\varphi} = \mu \left(\frac{\partial q_\varphi}{\partial r} - \frac{q_\varphi}{r} \right)$$

$$\tau_{\theta\varphi} = \frac{\mu}{r} \left(\frac{\partial q_\varphi}{\partial \theta} - \cot \theta q_\varphi \right)$$

The elastic energy per unit volume is given by

$$\tfrac{1}{2}\tau_{ij}\epsilon_{ij} = \frac{1}{4\mu} \{ \tau^2{}_{r\varphi} + \tau^2{}_{r\varphi} \}$$

$\tau_{r\varphi}$ is the stress associated with the traction on spherical surfaces. For the mantle bounded by free surfaces $\tau_{r\varphi}$ vanishes at both of the free surfaces. $\tau_{\theta\varphi}$ is the stress resulting from the twisting of a spherical shell, and it is associated with the differential rotation of conical sectors of a spherical shell. We will consider the energies associated with the radial stress, $\tau_{r\varphi}$, and the conical stress, $\tau_{\theta\varphi}$, separately.

In terms of the displacement, the energy associated with the radial stress is

$$\left(\frac{\tau_{r\varphi}\epsilon_{r\varphi}}{2} \right) = \frac{1}{4\mu} (P_l{}^1)^2 \left\{ \frac{\partial \, _n W_l}{\partial r} - \frac{_n W_l}{r} \right\}^2 \qquad (44)$$

The energy per unit thick spherical shell follows from integrating equation 44 over the spherical surface

$$\psi_r = \iint \frac{\tau_{r\varphi}\epsilon_{r\varphi}}{2} \, ds$$

$$= \frac{\pi r^2}{\mu} \frac{l(l+1)}{2l+1} \left\{ \frac{\partial \, _n W_l}{\partial r} + \frac{_n W_l}{r} \right\}^2$$

Similarly, the energy per unit volume associated with the conical stress is

$$\left(\frac{\tau_{r\varphi}\epsilon_{\theta\varphi}}{2} \right) = \frac{1}{r^2} (P_l{}^2)^2 \frac{1}{4\mu} \, _n W_l{}^2$$

and the energy contained within a spherical shell of unit thickness is

$$\psi_\theta = \iint \frac{\tau_{\theta\varphi}\epsilon_{\theta\varphi}}{2} \, ds$$

$$= \pi \frac{(l-1)l(l+1)(l+2)}{2l+1} \frac{1}{\mu} \, _n W_l{}^2(r)$$

The total energy $_n E_l$ associated with an oscillation of radial order n and angular order l is then

$$_n E_l = \pi \frac{l(l+1)}{2l+1} \int \frac{1}{\mu(r)} \left\{ \left(\frac{\partial \, _n W_l}{\partial r} + \frac{_n W_l}{r} \right)^2 \right.$$

$$\left. + (l-1)(l+2) \, _n W_l{}^2 \right\} r^2 \, dr \qquad (45)$$
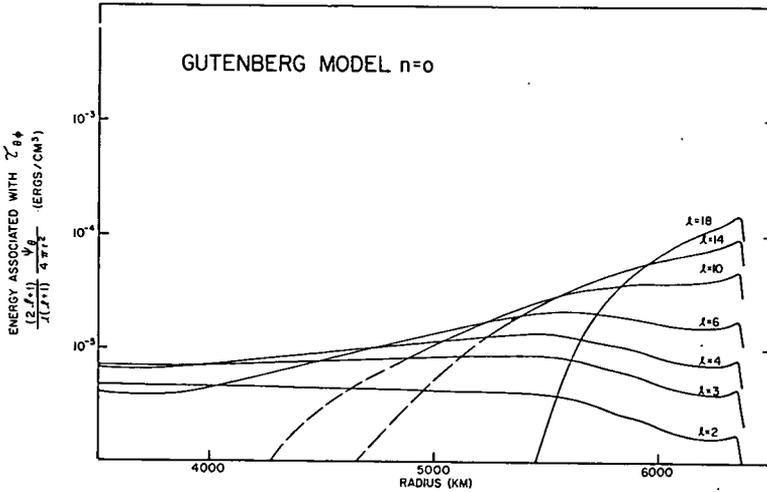
Fig. 16. Energy per unit volume associated with conical stress for Gutenberg model earth ($_0T_l$)

Equation 45 has been evaluated numerically for two models, a homogeneous mantle and a Gutenberg mantle (see part 6). Figure 7 illustrates the variation of the total elastic energy $_nE_l$ as a function of mode number l for the fundamental oscillations. The surface displacement is given by equation 43, and the energies are in ergs, assuming that the surface displacement is 1 cm. In progressing from $_0T_2$ to $_0T_{18}$ the elastic energy increases by about two orders of magnitude. The increase of energy with mode number l corresponds to the increased complexity in the pattern of displacement on the outer surface. Figure 8 lists the variation of total energy with l for the first overtone. For a given value of l the energy in the overtone is about two orders of magnitude greater than in the fundamental. For fixed surface displacement the energy increases with the overtone because of the increasing stresses required to produce the nodal surfaces within the earth.

An inhomogeneous earth with velocity and rigidity varying as the Gutenberg model has a lower energy in any given mode than a corre-
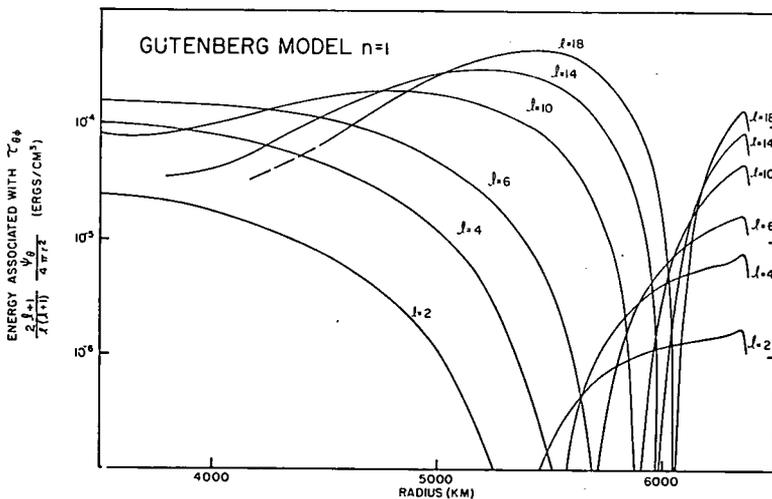
Fig. 17. Energy per unit volume associated with conical stress for Gutenberg model earth ($_1T_l$).
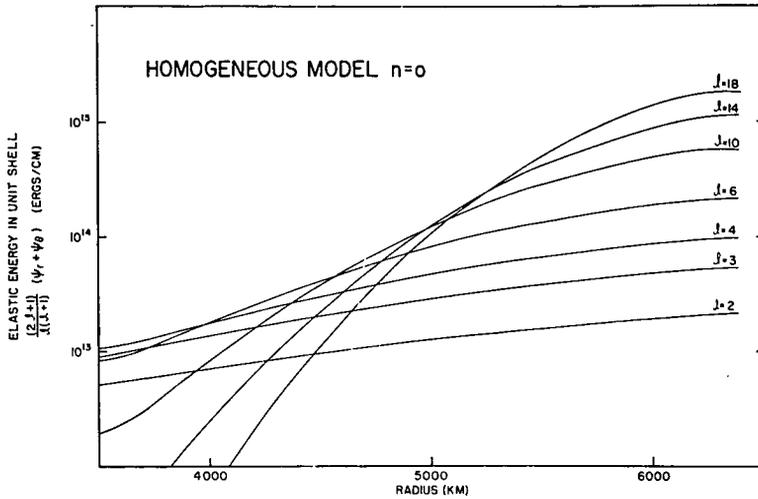
Fig. 18. Total elastic energy per unit radius for homogeneous model earth $(_0T_l)$.

sponding homogeneous mantle. This results partly from the fact that the Gutenberg model earth has a low-rigidity crust and upper mantle. It is possible to produce a given surface displacement in the inhomogeneous mantle with a lower stress than in a homogeneous mantle with a stiffer outer layer.

Figures 7 and 8 can be used to estimate the total elastic energy associated with a particular oscillation. As an example, we consider the $_0T_2$ oscillation excited by the Chilean earthquake. From the records obtained by *Benioff, Press, and Smith* [1961] the displacement is about 10^{-6} cm

(see part 4). Equation 42 then gives

$$_nW_l(a) \approx \frac{10^{-6}}{3\cos\theta\sin\theta} \approx 2\times 10^{-6} \quad \text{cm}$$

where we have taken the angular distance between Chile and Pasadena as 82°. The pattern of displacement rotates; the amplitude is period averaged. Assuming that $_0Q_2$ equals 200, the energy density corresponding to the $_0T_2$ oscillation for the Chilean earthquake is 10^{18} ergs/cph. Even though this figure is most uncertain it implies that the energy density must increase toward high frequencies if the total energy in
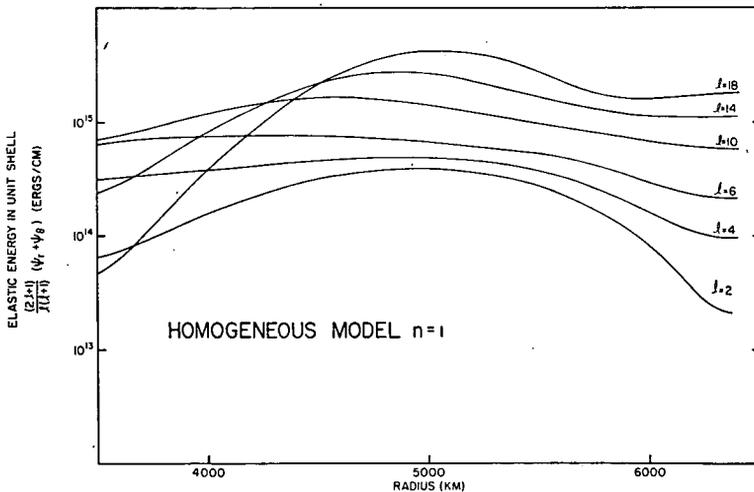
Fig. 19. Total elastic energy per unit radius for homogeneous model earth $(_1T_l)$.
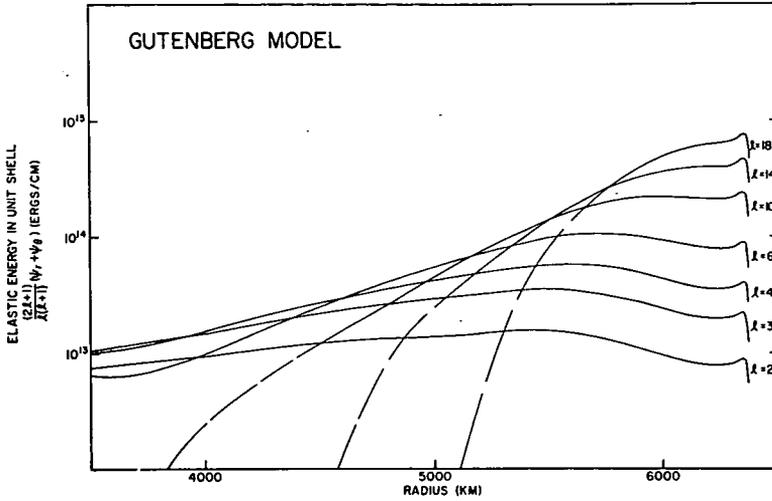
Fig. 20. Total elastic energy per unit radius for Gutenberg model earth ($_0T_l$).

the earthquake is of the order of 10^{24} ergs. A flat spectrum with the level of energy for the $_0T_2$ oscillation would require that the cutoff frequency be of the order of 10^3 cps. A lower cutoff frequency is more probable.

The above discussion suggests that it may be possible to obtain rough estimates of the energy in the lower-frequency toroidal oscillations for earthquakes recorded by instruments with known response curves. Corrections that must be made for the finite decay of the oscillations are straight-forward.

In Figure 9 we illustrate the variation of the normalized energy density associated with radial stress

$$\frac{(2l + 1)}{l(l + 1)} \frac{\psi_r}{4\pi r^2}$$

for a homogeneous mantle. The energy vanishes at both the core-mantle boundary and the outer surface because of the boundary conditions. The energy density is concentrated nearer the surface at higher mode numbers and is more evenly distributed throughout the mantle in the lower
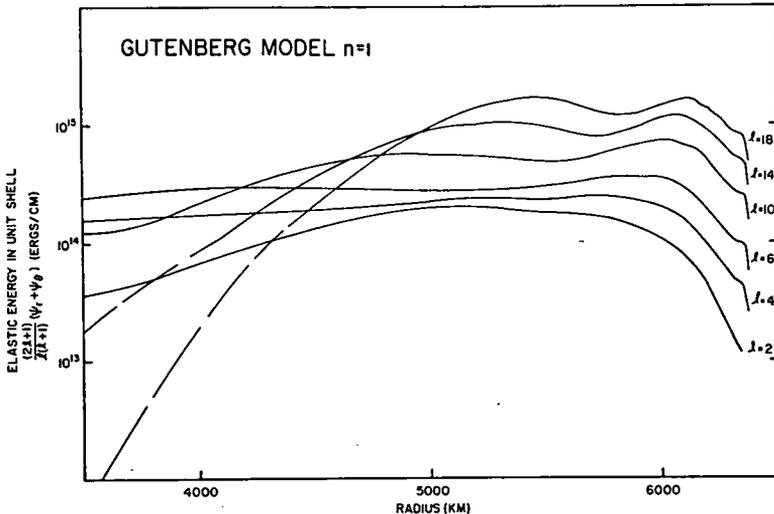
Fig. 21. Total elastic energy per unit radius for Gutenberg model earth ($_1T_l$).

mode numbers. Figure 10 illustrates the normalized energy density of the first overtones for a homogeneous earth. The level of energy is greater, but the features are similar in the sense that the energy in the higher modes tends to be concentrated toward the surface. Figures 11 and 12 illustrate the variation of the energy associated with the radial stress in the Gutenberg model for the fundamental and first overtone, respectively. As in the homogeneous model, the energy level increases toward the surface in the higher modes. The distribution is more irregular because of the nonuniform rigidity in the mantle.

The distribution of the normalized energy density

$$\frac{(2l + 1)}{l(l + 1)} \frac{1}{4\pi r^2} \psi_\theta$$

associated with the conical stress in a homogeneous mantle is shown in Figures 13 and 14. The energy in the fundamental (Fig. 13) is almost constant through the mantle for the low-order oscillations. The higher-order oscillations show a concentration of the energy toward the surface. The energy does not vanish at either the upper or lower surfaces since the boundary conditions involve the vanishing of the radial stress. In the overtone the energy associated with the conical stress vanishes at the radius corresponding to the radial nodal surface. The radial node approaches the surface with increasing mode number l. The variation of the depth to the radial node for the homogeneous and the Gutenberg model earth is shown in Figure 15.

The variation of the energy density associated with the conical stress for an inhomogeneous earth is shown in Figure 16 (fundamental) and Figure 17 (first overtone). The energy associated with the conical stress is lower in the crust because of the low rigidity of the crust, but the general features of the variation of this energy with depth are similar to those for the homogeneous earth. For the low-order modes the energy is uniformly distributed over the mantle for the fundamental and is concentrated toward the surface for the higher-order modes. The overtones again show the effect of the radial node.

The distribution of the normalized elastic energy per unit thick shell

$$\frac{(2l + 1)}{l(l + 1)} (\psi_r + \psi_\theta)$$

is shown in Figures 18 to 21. In Figure 18 the total energy per unit thick shell for a homogeneous earth is shown for the fundamental oscillations. At the low mode numbers the energy is evenly distributed throughout the mantle. At higher mode numbers there is a tendency for the concentration of energy toward the surface, though the peak in the near-surface concentration is not sharply defined. Figure 19 shows the distribution of energy for the first overtone in a homogeneous mantle. The energy tends to be concentrated about halfway through the mantle. The node in the upper part of the mantle associated with the conical stress decreases the energy in the upper mantle, and the lower energy near the core-mantle boundary combines to produce the peak in the energy near the central part of the mantle.

The distribution of total energy per unit thick shell in an inhomogeneous earth resembles that in a homogeneous earth. Figure 20 illustrates the distribution of energy in the Gutenberg model for the fundamental oscillations. The low-order oscillations have more or less constant energy throughout the mantle. It should be noted that the small dip in the energy curves near the upper mantle implies that the low-order oscillations are somewhat insensitive to the region of low velocity in the mantle. For higher-order oscillations the energy is more nearly concentrated toward the surface. For $_0T_{10}$ the energy drops to one-half the peak value at 900-km depth. For $_0T_{14}$ the depth at which the elastic energy is one-half peak value is 700 km; for $_0T_{18}$, it is 520 km.

The results shown in Figure 20 clearly illustrate the fact that the low-order oscillations uniformly sample the entire mantle; the low-order resonant frequencies of the inhomogeneous earth and the homogeneous mantle are almost identical. For $l = 6$ the lower part of the mantle is less important in determining the resonant frequency, since the energy distribution begins to drop off rapidly at a depth of some 1500 km. These results imply that the study of the detailed characteristics of the upper mantle will depend on the identification and analysis of toroidal oscillations of order 15 to 30, corresponding to a range in periods of 9 to 4 minutes. These high-order oscillations will provide definitive evidence on the variation of rigidity in the critical upper region of the mantle.

The results presented in Figure 20 will also

be useful in the interpretation of the anelastic properties of the mantle. The Q obtained from the $_0T_2$ oscillation will provide the average anelastic properties for pure shear in the mantle. The major contribution to the Q obtained for the $_0T_{13}$ oscillation will come from the upper 500 km of the mantle. We should thus be able to obtain an estimate of the distribution of the dissipative properties in the mantle. An attempt to study the amplitude decay of the toroidal oscillations with time has been made on the Lamont record. The record is too short to give definitive results, but the value obtained for $_0Q_8$ is 250 and that for $_0Q_{10}$ is 200.

Figure 21 shows the variation of total elastic energy per unit thick shell for the first overtones in the Gutenberg model earth. As in the homogeneous mantle there is a tendency for the energy to be concentrated near the center of the mantle as a result of the node in the conical stress in the upper part of the mantle.

6. MODEL CALCULATION

The resonant frequencies of the toroidal oscillations for $l = 2$-17 and $n = 0$-3 have been computed for a number of earth models. An earth model is defined by the radial distribution of shear-wave velocity C_S and rigidity μ. The discrepancy between observed and calculated resonant frequencies provides a measure of the uncertainty in our knowledge of the constitution of the mantle. The computations used the radial distribution of elastic energy (see part 5) for a given oscillation as a guide in adjusting earth models to fit the observed frequencies. The majority of the calculations are based on the assumption that the earth's mantle is bounded by two free surfaces. Additional solutions have been obtained in which the core-mantle boundary is taken as rigid. This study is necessary to investigate the effect of the core-mantle boundary on the toroidal oscillations (see part 4).

The starting point for the calculations is an assumed model of the earth's mantle derived from classical seismology. We have initially considered two models, the Gutenberg and the Lehmann. Both these models are characterized by having a layer of lower velocity in the upper mantle; this layer distinguishes these models from Bullen's model A or model B. Comparison of theoretical and observed spheroidal oscillations [*Pekeris, Alterman, and Jarosch*, 1961] shows

that the observations favor the Gutenberg model over Bullen B. Moreover, a number of seismic studies provide support for the existence of a low-velocity layer (see part 7).

The actual computation of the resonant frequencies has been carried out by the method described by *Gilbert and MacDonald* [1960]. The earth is assumed to be made up of a number of concentric spherical elastic shells. The motion in each shell is described by a sum of products of surface spherical harmonics and spherical Bessel functions. The solutions for each shell are continued by use of the continuity condition on the stress and displacement. The resonant frequencies are obtained by applying the boundary conditions at the outer and inner surface. For the mantle bounded by free surfaces, the boundary conditions are symmetrical and require that the radial traction

$$R_i = \sum_{l=1}^{\infty} \sum_{m=-l}^{l} \sqrt{l(l+1)} \; C^m{}_{i,l}$$
$$\cdot \{\mu k A_{lm}[j_l'(kr) - (kr)^{-1}j_l(kr)]$$
$$+ \mu k B_{lm}[y_l'(kr) - (kr)^{-1}y_l(kr)]\}$$
$$k = \omega(\rho/\mu)^{1/2}$$

vanishes on the outer surface and at the core-mantle boundary. For the case of a stiff lower boundary we obtain the resonant frequencies by requiring that the radial traction vanish at the outer boundary and the displacement vanish over the core-mantle boundary. The details of the matrix operations used in the actual numerical calculations are described by *Gilbert and MacDonald* [1960].

A homogeneous mantle is taken as a basis for comparison in much of the following discussion. It is defined as a spherical shell with inner radius of 3472 km and outer radius of 6371 km. The elastic properties are

$$C_S = 6.24 \text{ km/sec}$$
$$\mu = 1.74 \times 10^{12} \text{ dynes/cm}^2 \quad \rho = 4.47 \text{ g/cm}^3$$

corresponding to the mass-average properties of Bullen's model B. The resonant frequencies for the oscillations $_0T_l$ are listed in Table 11. The resonant frequencies for the higher overtones $n = 1, 2$, and 3 are summarized in Tables 12, 13, and 14.

The calculation of the distribution of elastic

TABLE 9. Parameters for Gutenberg Model Earths

Radius, km × 10⁻³	Gutenberg		Gutenberg I		Gutenberg IV		Gutenberg V		Gutenberg Low Density, μ, megabars
	C_s, km/sec	μ, megabars	C_s, km/sec	μ, megabars	C_s, km/sec	μ, megabars	C_s, km/sec	μ, megabars	
3.47	7.20	2.95	7.11	2.88	Same as	Same as	7.08	2.86	Same as
3.57	7.23	2.92	7.14	2.85	Guten-	Guten-	7.11	2.83	Gutenberg
3.77	7.15	2.81	7.06	2.74	berg I	berg I	7.03	2.72	to
3.97	7.05	2.68	6.94	2.62	to	to	6.91	2.60	$R = 6.02$
4.17	6.97	2.57	6.88	2.51	$R = 5.87$	$R = 5.87$	6.85	2.49	$\times 10^3$
4.37	6.90	2.47	6.81	2.41	$\times 10^3$	$\times 10^3$	6.78	2.39	
4.57	6.80	2.34	6.72	2.28			6.69	2.26	
4.77	6.69	2.22	6.61	2.17			6.58	2.15	
4.97	6.55	2.08	6.47	2.03			6.44	2.01	
5.17	6.42	1.95	6.34	1.90			6.31	1.88	
5.37	6.32	1.85	6.24	1.80			6.21	1.78	
5.47	6.23	1.77	6.15	1.72			6.12	1.70	
5.57	6.03	1.60	5.96	1.56			5.93	1.54	
5.67	5.76	1.40	5.69	1.34			5.66	1.32	
5.72	5.45	1.19	5.38	1.16			5.38	1.14	
5.87	5.20	1.04	5.14	1.01			5.16	1.03	
5.92	5.04	0.937	4.98	0.914	5.00	0.924	5.02	0.944	
5.97	4.85	0.852	4.79	0.831	4.82	0.814	4.84	0.824	
6.02	4.68	0.784	4.62	0.765	4.66	0.780	4.68	0.800	0.773
6.07	4.54	0.728	4.48	0.710	4.52	0.720	4.54	0.740	0.707
6.12	4.46	0.696	4.41	0.679	4.46	0.679	4.48	0.710	0.676
6.15	4.42	0.680	4.37	0.664	4.42	0.680	4.44	0.700	0.660
6.17	4.38	0.664	4.33	0.648	4.38	0.664	4.40	0.684	0.646
6.20	4.36	0.652	4.31	0.636	4.36	0.652	4.38	0.672	0.639
6.22	4.35	0.645	4.30	0.629	4.35	0.645	4.37	0.665	0.634
6.25	4.37	0.647	4.32	0.631	4.37	0.647	4.39	0.667	0.640
6.27	4.41	0.657	4.36	0.641	4.41	0.657	4.43	0.677	0.651
6.28	4.46	0.670	4.41	0.654	4.46	0.670	4.48	0.690	0.666
6.29	4.51	0.683	4.46	0.667	4.51	0.683	4.53	0.703	0.681
6.30	4.57	0.700	4.51	0.683	4.57	0.700	4.59	0.720	0.689
6.31	4.60	0.713	4.54	0.696	4.60	0.713	4.62	0.733	0.715
6.32	4.65	0.718	4.59	0.701	4.65	0.718	4.67	0.738	0.724
6.34	3.80	0.433	3.75	0.423	3.80	0.433	3.80	0.433	0.433
6.35	3.55	0.345	3.51	0.337	3.55	0.345	3.55	0.345	0.345

Gutenberg II:　　　　　$C_s = C_s$ of Gutenberg I.
　　　　　　　　　　$\mu = \mu$ of Gutenberg.
Gutenberg III:　　　　$C_s = C_s$ of Gutenberg.
　　　　　　　　　　$\mu = \mu$ of Gutenberg I.
Gutenberg low-density: $C_s = C_s$ of Gutenberg.

energy associated with a single oscillation shows that the $_0T_2$, $_0T_3$, and $_0T_4$ modes should give a good estimate of the mass-averaged velocity and rigidity for the mantle, provided that boundary effects are unimportant. The $_0T_2$ oscillation is, however, perturbed by a core-mantle interaction; hence the $_0T_3$ oscillation gives the best estimate. The values listed in Table 11 show that the observed period of $_0T_3$ is about 1 per cent larger than the calculated period for the homogeneous mantle. In the homogeneous mantle the period varies inversely with the shear-wave velocity so that the average shear-wave velocity for the mantle should be 6.18 km/sec. The mass-average rigidity of the earth's mantle is somewhat less than that for Bullen's model B. The accurate determination of the frequencies of the low-order oscillations and therefore of the mass-average properties of the mantle can be used to fix the total mass of the mantle within

density. For the purposes of this calculation, the difference is unimportant, as will be shown below.

The effect of the inhomogeneous distribution of rigidity and density on the resonant frequencies is illustrated in Figure 22, where the frequencies for the Gutenberg and homogeneous models are shown. For oscillations of orders 2, 3, and 4, the frequencies are very nearly the same; the elastic energy associated with these oscillations is uniformly distributed throughout the mantle. The higher-order oscillations predominantly sample shallower regions of the upper mantle. In the Gutenberg model the average rigidity of the upper mantle is less than the rigidity for the mantle as a whole. The frequencies are therefore lower than for the homogeneous mantle. The frequency interval between different mode numbers becomes less at a greater rate in the Gutenberg model than in the homogeneous model. This is a consequence of the lower rigidity and shear-wave velocity of the Gutenberg model in the upper part of the mantle.

Fig. 22. Comparison of resonant frequencies in Gutenberg and homogeneous model earth $(_0T_l)$.

about 1 per cent. This accuracy or greater is required in order to investigate the question of the total mass contained within the earth's inner core. The average density of the outer core is known within 5 per cent, but the density of the inner core, occupying only 0.7 per cent of the volume of the earth, is unknown.

The elastic parameters defining the Gutenberg model earth are listed in Table 9 [*Bullen*, 1959; *Dorman, Ewing, and Oliver*, 1960, *Pekeris, Alterman, and Jarosch*, 1961]. In the Gutenberg model the shear-wave velocity initially decreases, beginning at the base of the crust, and reaches a minimum at a depth of 150 km. The rigidities used in these calculations are those listed by Bullen, but they are undoubtedly inappropriate for the upper part of the mantle. As is discussed in part 7, the density most probably remains constant or decreases slightly within the upper layers of the mantle, while the listed values of the rigidity imply a monotonically increasing

Fig. 23. Comparison of resonant frequencies in Gutenberg and homogeneous model earth $(_1T_l)$.

MacDONALD AND NESS

TABLE 10. Parameters for Lehmann Model Earths

Radius, km $\times$ 10^{-3}	Lehmann		Lehmann I		Lehmann II		Lehmann Velocity— Bullen B Density μ, megabars
	C_s, km/sec	μ, megabars	C_s, km/sec	μ, megabars	C_s, km/sec	μ, megabars	
3.47	7.30	3.03	Same as	Same as	Same as	Same as	2.86
3.50	7.30	3.02	Lehmann	Lehmann	Lehmann	Lehmann	2.85
3.55	7.30	3.01	to	to	to	to	2.83
3.60	7.28	2.98	$R = 5.98$	$R = 5.98$	$R = 5.85$	$R = 5.85$	2.81
3.65	7.26	2.95	$\times$ 10^3	$\times$ 10^3	$\times$ 10^3	$\times$ 10^3	2.78
3.70	7.24	2.93					2.75
3.75	7.22	2.90					2.72
3.80	7.20	2.87					2.69
3.85	7.18	2.83					2.66
3.90	7.15	2.80					2.63
3.95	7.12	2.77					2.60
4.00	7.10	2.74					2.57
4.05	7.08	2.70					2.54
4.10	7.05	2.67					2.51
4.15	7.03	2.63					2.49
4.20	7.00	2.60					2.46
4.25	6.98	2.57					2.43
4.30	6.96	2.55					2.40
4.35	6.94	2.52					2.38
4.40	6.91	2.49					2.35
4.45	6.89	2.46					2.33
4.50	6.86	2.43					2.30
4.55	6.84	2.40					2.27
4.60	6.82	2.37					2.25
4.65	6.80	2.35					2.23
4.70	6.77	2.32					2.20
4.75	6.74	2.29					2.16
4.80	6.71	2.26					2.13
4.85	6.68	2.23					2.10
4.90	6.65	2.20					2.07
4.95	6.62	2.16					2.04
5.00	6.60	2.13					2.02
5.05	6.58	2.10					1.99
5.10	6.54	2.07					1.96
5.15	6.50	2.03					1.93
5.20	6.47	2.00					1.90
5.25	6.44	1.97					1.87
5.30	6.41	1.94					1.84
5.35	6.37	1.90					1.81
5.40	6.33	1.86					1.77
5.45	6.29	1.82					1.74
5.50	6.23	1.77					1.70
5.55	6.16	1.71					1.65
5.60	6.08	1.64					1.59
5.65	5.97	1.55					1.52
5.70	5.84	1.46					1.45
5.75	5.71	1.36					1.38
5.80	5.56	1.26					1.30
5.85	5.41	1.16					1.23
5.90	5.25	1.05			5.18	1.05	1.14
5.92	5.18	1.01			5.05	0.990	1.10
5.94	5.11	0.968			4.90	0.930	1.07
5.96	5.05	0.928			4.78	0.870	1.04
5.98	4.92	0.880			4.72	0.810	0.983
6.00	4.90	0.866	4.94	0.850	4.67	0.770	0.927

TABLE 10. Continued

Radius, km × 10⁻³	Lehmann		Lehmann I		Lehmann II		Lehmann Velocity—Bullen B Density μ, megabars
	C_s, km/sec	μ, megabars	C_s, km/sec	μ, megabars	C_s, km/sec	μ, megabars	
6.02	4.87	0.853	4.90	0.790	4.64	0.730	0.868
6.04	4.84	0.840	4.81	0.740	4.64	0.730	0.811
6.06	4.82	0.830	4.72	0.700	4.64	0.730	0.790
6.08	4.80	0.815	4.64	0.670	4.64	0.730	0.783
6.10	4.77	0.802	4.56	0.640	4.64	0.730	0.773
6.12	4.74	0.790	4.48	0.620	4.64	0.730	0.764
6.14	4.71	0.778	4.39	0.610	4.64	0.730	0.754
6.16	4.30	0.640	4.30	0.610	4.64	0.730	0.629
6.18	4.30	0.637	4.23	0.610	4.64	0.730	0.629
6.20	4.30	0.634	4.30	0.615	4.64	0.730	0.629
6.22	4.30	0.631	4.38	0.620.	4.64	0.730	0.629
6.24	4.30	0.628	4.48	0.640	4.64	0.730	0.629
6.26	4.64	0.730	4.56	0.690	4.64	0.730	0.730
6.28	4.63	0.720	4.63	0.720	4.63	0.720	0.720
6.30	4.62	0.712	4.62	0.712	4.62	0.712	0.712
6.32	4.61	0.706	4.61	0.706	4.61	0.706	0.706
6.34	4.60	0.684	4.60	0.684	4.60	0.684	0.684
6.36	3.60	0.369	3.60	0.369	3.60	0.369	0.369

Lehmann III: $C_s = C_s$ of Lehmann.
             $\mu = 0.98\,\mu$ of Lehmann.
Lehmann IV: $C_s = C_s$ of Lehmann.
             $\mu = 1.02\,\mu$ of Lehmann.
Lehmann velocity Bullen B density: $C_s = C_s$ of Lehmann.

Figure 23 illustrates the frequencies for the first overtone for both the inhomogeneous Gutenberg model and the homogeneous model. The distribution of frequencies is more complex than in the case of the fundamentals because of the nodal surface for the energy associated with the conical stress. The $_1T_2$ oscillation has a higher frequency in the Gutenberg than in the homogeneous model, since the energy in the first overtone is concentrated in the lower regions of the mantle with a greater C_s. The first overtones of orders 11 and 12 have nearly identical periods for the Gutenberg and homogeneous models and depend only on the mass-averaged properties.

The periods calculated for the Gutenberg model are 1 to 2 per cent lower than the observed periods. The difference is consistent and is larger than combined uncertainties of the computation and observations. As a measure of the agreement of the theoretical models with the observations, we use the quantity

$$D = \sum_l \frac{|T_l^{(obs)} - T_l^{(model)}|}{T_l^{(obs)}}$$

where $T_l^{(obs)}$ is the observed period for the

toroidal oscillation of order l; the summation extends over the observed oscillations.

Table 15 lists the value of D for various models in decreasing order of agreement with observation. The observed values used in constructing Table 15 are those derived from our analysis of the Lamont strain seismograph (see Table 1). $_0T_2$ is not present on the record; it is not included in the listing of the observations. The average percentage deviation over the eleven observed toroidal modes is about 1 per cent for the Gutenberg model. We also note that the inhomogeneous model is far superior to the homogeneous model.

The actual mantle is somewhat less rigid than that assumed in the Gutenberg model. Gutenberg I is an attempt to fit the observations by uniformly lowering the shear-wave velocity by 1.2 per cent and the rigidity by 2.4 per cent. The periods are increased, and the fit to the observations is better (see Table 15). The comparative effect of variations of rigidity and velocity are illustrated in Gutenberg II and Gutenberg III. Gutenberg II maintains the same rigidity as Gutenberg, but the velocity is identical to that of Gutenberg I. Since $\rho = \mu/C_s^2$, the

MacDONALD AND NESS

TABLE 11. Resonant Periods in Minutes for $_0T_l$

$N = 0$	$L = 2$	3	4	5	6	7	8	9
Observations		28.570	21.950	18.020	15.510	13.750	12.350	11.240
Gutenberg IV	44.106	28.548	21.864	18.040	15.525	13.721	12.351	11.265
Gutenberg II	44.181	28.602	21.912	18.084	15.567	13.763	12.392	11.307
Gutenberg V	44.062	28.498	21.803	17.971	15.448	13.640	12.265	11.177
Gutenberg I	44.170	28.598	21.910	17.649	15.165	13.765	12.395	11.310
Gutenberg III	43.626	28.244	21.640	17.861	15.377	13.596	12.243	11.171
Gutenberg low-density	43.581	28.213	21.612	17.836	15.353	13.574	12.222	11.152
Gutenberg	43.631	28.247	21.642	17.861	15.376	13.594	12.241	11.169
Gutenberg stiff	32.150	25.237	21.032	17.527	15.258	13.553	12.226	11.164
Lehmann velocity Bullen density	43.671	28.245	21.603	17.794	15.282	13.479	12.109	11.024
Lehmann III	43.322	28.045	21.458	17.683	15.199	13.417	12.064	10.930
Lehmann I	43.205	27.927	21.356	17.599	15.125	13.351	12.017	10.951
Lehmann II	43.314	28.013	21.423	17.654	15.171	13.389	12.047	10.974
Lehmann	43.332	28.022	21.429	17.657	15.173	13.390	12.046	10.972
Lehmann IV	43.310	28.007	21.422	17.652	15.171	13.383	12.030	10.960
Homogeneous	44.351	28.250	21.229	17.169	14.487	12.569	11.121	9.985
Homogeneous stiff	35.270	25.903	20.422	16.856	14.358	12.514	11.098	9.974

$N = 0$	$L = 10$	11	12	13	14	15	16	17
Observations	10.330	9.614	9.065		7.985			
Gutenberg IV	10.380	9.640	9.010	8.467	7.991	7.573	7.200	6.854
Gutenberg II	10.421	9.682	9.052	8.508	8.032	7.612	7.244	
Gutenberg V	10.290	9.548	8.918	8.374	7.898	7.479	7.104	6.770
Gutenberg I	10.424	9.684	9.055	8.511	8.035	7.615	7.246	6.892
Gutenberg III	10.299	9.566	8.944	8.407	7.937	7.522	7.155	6.822
Gutenberg low density	10.279	9.550	8.930	8.394	7.925	7.512	7.144	6.817
Gutenberg	10.294	9.563	8.941	8.404	7.934	7.520	7.150	6.811
Gutenberg stiff	10.293	9.564	8.943	8.406	7.936	7.520	7.151	6.811
Lehmann velocity Bullen density	10.140	9.402	8.776	8.236	7.765	7.349	7.037	6.722
Lehmann III	10.120	9.391	8.772	8.238	7.772	7.358	7.001	6.670
Lehmann I	10.089	9.365	8.747	8.236	7.984	7.359	7.000	6.670
Lehmann II	10.105	9.375	8.752	8.219	7.759	7.340	6.906	6.657
Lehmann	10.103	9.373	8.752	8.233	7.756	7.341	6.971	6.663
Lehmann IV	10.087	9.359	8.741	8.208	7.743	7.333	6.968	6.900
Homogeneous	9.068	8.310	7.672	7.128	6.657	6.246	5.884	5.563
Homogeneous stiff	9.063	8.307	7.671	7.127	6.657	6.246	5.884	5.562

density at each point in Gutenberg II is greater by 2.4 per cent than the density in Gutenberg. Maintaining the rigidity constant but everywhere lowering the velocity 1.2 per cent over that in the Gutenberg model increases the periods by a greater amount than increasing both the rigidity and the velocity. Gutenberg II provides a better fit to the observations than the unadjusted Gutenberg model.

In Gutenberg III the velocity distribution is that of the Gutenberg model, but the rigidity is that of Gutenberg I (2.4 per cent lower than in the Gutenberg model). The density at every point in Gutenberg III is less than the density in the Gutenberg model by 2.4 per cent. The variation in rigidity produces only a slight alteration in the period. The $_0T_5$ oscillation of Gutenberg II equals that of Gutenberg; oscilla-

TABLE 12.   Resonant Periods in Minutes for $_1T_l$

$N = 1$	$L = 2$	3	4	5	6	7	8	9
Gutenberg IV	12.749	11.690	10.606	9.602	8.725	7.983	7.363	6.845
Gutenberg II	12.755	11.695	10.611	9.606	8.729	7.988	7.368	6.850
Gutenberg V	12.764	11.704	10.619	9.614	8.665	7.992	7.371	6.851
Gutenberg I	12.762	11.701	10.616	9.387	8.528	7.991	7.371	6.853
Gutenberg III	12.599	11.552	10.480	9.489	8.623	7.891	7.279	6.768
Gutenberg low-density	12.575	11.532	10.465	9.477	8.614	7.884	7.274	6.764
Gutenberg	12.593	11.546	10.474	9.484	8.619	7.888	7.276	6.765
Gutenberg stiff	10.033	9.601	9.102	8.575	8.052	7.552	7.088	6.664
Lehmann velocity								
Bullen density	12.528	11.463	10.381	9.584	8.517	7.843	7.174	6.664
Lehmann III	12.520	11.471	10.401	9.414	8.553	7.825	7.217	6.709
Lehmann I	12.456	11.422	10.426	9.389	8.537	7.814	7.214	6.713
Lehmann II	12.504	11.460	10.392	9.408	8.551	7.825	7.213	6.712
Lehmann	12.505	11.453	10.386	9.400	8.540	7.811	7.205	7.272
Lehmann IV	12.484	11.439	10.373	9.387	8.530	7.802	7.195	6.687
Homogeneous	13.116	12.016	10.900	9.862	8.943	8.148	7.468	6.889
Homogeneous stiff	10.236	9.765	9.226	8.665	8.111	7.585	6.125	6.646

$N = 1$	$L = 10$	11	12	13	14	15	16	17
Gutenberg IV	6.406	6.030	5.703	5.414	5.157	4.926	4.716	4.526
Gutenberg II	6.412	6.037	5.710	5.421	5.164	4.933	4.723	4.533
Gutenberg V	6.411	6.035	5.707	5.417	5.160	4.928	4.731	4.528
Gutenberg I	6.414	6.038·	5.710	5.421	5.164	4.932	4.723	4.532
Gutenberg III	6.335	5.963	5.640	5.355	5.100	4.872	4.665	4.477
Gutenberg low-density	6.333	5.963	5.641	5.357	5.103	4.876	4.669	4.482
Gutenberg	6.333	5.962	5.639	5.354	5.100	4.872	4.665	4.477
Gutenberg stiff	6.281	5.936	5.627	5.349	5.098	4.871	4.665	4.478
Lehmann velocity								
Bullen density	6.234	5.867	5.548	5.268	5.020	4.796	4.595	4.412
Lehmann III	6.279	5.910	5.589	5.306	5.053	4.826	4.620	4.433
Lehmann I	6.289	5.925	5.608	5.328	5.077	4.884	4.647	4.460
Lehmann II	6.284	5.917	5.597	5.314	5.063	4.836	4.628	4.443
Lehmann	6.270	5.902	5.582	5.299	5.048	4.821	4.616	4.429
Lehmann IV	6.258	5.891	5.571	5.289	5.038	4.812	4.608	
Homogeneous	6.393	5.967	5.599	5.277	4.993	4.740	4.496	4.309
Homogeneous stiff	6.240	5.872	5.541	5.242	4.972	4.728	4.507	4.305

tions of lower order have a shorter period, and oscillations of greater l have a longer period. The resonant frequencies are thus determined primarily by the velocity distribution and to a much lesser extent by the distribution of rigidity. The rigidity enters into the determination of the periods only because of the variation of velocity with depth.

The model that fits the observations best is Gutenberg IV (see Table 15). In this model the distribution of velocity and rigidity is taken to be the same as that of Gutenberg I from the core-mantle boundary to a depth of 500 km. At this depth the distribution is joined smoothly to the Gutenberg distribution. The velocity in the deeper part of the mantle is less than in the Gutenberg model but in the upper part of the mantle is equal to that in the Gutenberg model. The $_0T_2$ oscillation in this model has a period 0.5 minute longer than that in the Gutenberg model.

The total deviation from the observations is less than 3 per cent in this model. It should be emphasized that this model is not unique. Other variations of the Gutenberg model are possible

MacDONALD AND NESS

TABLE 13. Resonant Periods in Minutes for $_2T_l$

$N = 2$	$L = 2$	3	4	5	6	7	8	9
Gutenberg IV	7.492	7.316	7.053	6.753	6.429	6.093	5.757	5.434
Gutenberg II	7.533	7.322	7.059	6.760	6.435	6.099	5.763	5.439
Gutenberg V	7.527	7.316	7.055	6.756	6.434	6.099	5.765	5.442
Gutenberg I	7.536	7.348	7.065	6.581	6.271	6.099	5.763	5.438
Gutenberg III	7.442	7.233	6.973	6.676	6.354	6.021	5.689	5.368
Gutenberg low-density	7.437	7.229	6.971	6.675	6.355	6.023	5.692	5.372
Gutenberg	7.440	7.231	6.971	6.674	6.354	6.021	5.689	5.369
Gutenberg stiff	6.285	6.167	6.018	5.846	5.655	5.452	5.244	5.034
Lehmann velocity Bullen density	7.280	7.079	6.830	6.546	6.240	5.923		5.301
Lehmann III	7.362	7.156	6.901	6.609	6.294	5.968	5.642	5.328
Lehmann I	7.368	7.166	6.914	6.620	6.314	6.011	5.664	5.351
Lehmann II	7.377	7.170	6.916	6.624	6.308	5.982	4.452	5.340
Lehmann	7.345	7.140	6.887	6.598	6.284	5.960	5.636	5.323
Lehmann IV	7.323	7.120	6.869	6.584	6.273	5.948	5.626	5.315
Homogeneous	7.393	7.195	6.951	6.677	6.385	6.084	5.783	5.489
Homogeneous stiff	6.175	6.069	5.927	5.766	5.590	5.403	5.210	5.015

$N = 2$	$L = 10$	11	12	13	14	15	16	17
Gutenberg IV	5.130	4.851	4.601	4.376	4.176	3.998	3.837	3.692
Gutenberg II	5.135	4.856	4.605	4.381	4.181	4.002	3.842	3.697
Gutenberg V	5.139	4.861	4.610	4.385	4.185	4.006	3.845	3.699
Gutenberg I	5.134	4.855	4.604	4.380	4.159	4.002	3.841	3.693
Gutenberg III	5.068	4.793	4.584	4.324	4.127	3.951	3.793	3.645
Gutenberg low-density	5.072	4.797	4.550	4.329	4.132	3.956	3.798	3.655
Gutenberg	5.069	4.794	4.546	4.325	4.128	3.952	3.794	3.651
Gutenberg Stiff	4.828	4.628	4.437	4.256	4.086	3.927	3.780	3.643
Lehmann velocity Bullen density	5.014	4.750	4.499	4.298	4.108	3.937	3.782	3.642
Lehmann III	5.033	4.762	4.519	4.301	4.106	3.990	3.768	3.633
Lehmann I	5.056	4.786	4.540	4.324	4.173	3.956	3.799	3.655
Lehmann II	5.044	4.773	4.530	4.312	4.117	3.941	3.785	3.641
Lehmann	5.028	4.779	4.516	4.298	4.105	3.935	3.774	3.632
Lehmann IV	5.023	4.755	4.512	4.296	4.102	3.929	3.772	
Homogeneous	5.206	4.939	4.688	4.456	4.243	4.047	3.869	3.706
Homogeneous stiff	4.886	4.634	4.451	4.276	4.108	3.950	3.800	3.659

in which agreement with observation is comparable. We believe, however, that the improvement in Gutenberg IV over the Gutenberg model is real, and that the model eventually adopted for the mantle will be characterized by a lower average shear-wave velocity than the Gutenberg model. The shear-wave velocities in the Gutenberg model for the lower mantle are about 1 per cent too high. Gutenberg IV is not satisfactory in the sense that it gives an increasing density with depth, which is incompatible with concepts of a chemically homogeneous low-velocity layer.

Two additional models have been constructed. In the Gutenberg low-density model the velocity is the same as in the Gutenberg model but the density is adjusted to remain constant over the low-velocity region. The rigidity is joined smoothly to the Gutenberg model at a depth of 350 km. This model is nearly identical to the Gutenberg model, since the change in density varies only the rigidity. Furthermore, these variations take place only in the upper part of the mantle and thus influence lower oscillations to a slight degree. A study of the higher oscillations is required to determine the distribution of

TABLE 14. Resonant Periods in Minutes for $_3T_l$

$N = 3$	$L = 2$	3	4	5	6	7	8	9
Gutenberg IV	5.187	5.115	5.023	4.914	4.790	4.654	4.509	4.358
Gutenberg II	5.195	5.124	5.031	4.921	4.797	4.660	4.515	4.364
Gutenberg V	5.189	5.118	5.026	4.917	4.794	4.659	4.515	4.364
Gutenberg I	5.193	5.121	5.029	4.821	4.795	4.659	4.514	4.363
Gutenberg III	5.129	5.058	4.967	4.859	4.736	4.601	4.458	4.309
Gutenberg low-density	5.138	5.067	4.975	4.867	4.743	4.609	4.465	4.315
Gutenberg		5.060	4.969	4.861	4.738	4.603	4.594	
Gutenberg stiff	4.469	4.424	4.366	4.296	4.216	4.128	4.034	3.935
Lehmann velocity								
Bullen density		5.013	4.926	4.822	4.704	4.574	4.436	4.290
Lehmann III	5.097	5.027	4.938	4.831	4.710	4.577	4.435	4.287
Lehmann I	5.141	5.072	4.903	4.873	4.750	4.615	4.471	4.320
Lehmann II	5.119	5.052	4.961	4.853	4.730	4.596		4.302
Lehmann	5.084	5.023	4.934	4.828	4.707	4.575	4.433	4.285
Lehmann IV	5.084	5.015	4.926	4.823	4.701	4.569	4.429	4.282
Homogeneous		4.993	4.912	4.817	4.708	4.590	4.464	4.334
Homogeneous stiff	4.418	4.377	4.324	4.261	4.188	4.062	4.021	3.944

$N = 3$	$L = 10$	11	12	13	14	15	16	17
Gutenberg IV	4.204	4.048	3.893	3.741	3.596	3.457	3.328	3.209
Gutenberg II	4.209	4.052	3.897	3.745	3.599	3.461	3.332	3.212
Gutenberg V	4.210	4.055	3.901	3.749	3.603	3.465	3.336	3.216
Gutenberg I	4.208	4.052	3.897	3.745		3.461	3.332	3.213
Gutenberg III	4.156	4.001		3.698	3.553	3.416	3.289	3.171
Gutenberg low-density	4.161	4.006	3.852	3.702	3.557	3.420	3.292	3.174
Gutenberg	4.156	4.001	3.848	3.697	3.553	3.416	3.288	3.171
Gutenberg stiff	3.832	3.728	3.622	3.518	3.414	3.314	3.215	3.120
Lehmann velocity								
Bullen density	4.140	3.988	3.861	3.687	3.543	3.406	3.279	3.161
Lehmann III	4.133	3.980			3.533	3.396		3.160
Lehmann I	4.171	4.007	3.851	3.698	3.551	3.432	3.283	3.164
Lehmann II	4.147	3.991	3.836	3.684	3.539	3.401	3.272	3.153
Lehmann	4.133		3.826	3.551	3.532		3.267	3.149
Lehmann IV	4.130	3.977	3.825	3.675	3.531	3.395	3.267	
Homogeneous	4.200	4.065	3.930	3.796	3.665	3.536	3.412	3.292
Homogeneous stiff	3.834	3.737	3.639		3.442	3.346	3.251	3.158

velocity and elastic parameters in the upper part of the mantle. Gutenberg V is a perturbation on the Gutenberg IV model in which the velocity is 0.5 per cent greater in the upper 400 km (see Table 9). The agreement of the Gutenberg V model with observations is not as good as that of Gutenberg IV.

Another class of earth models has been constructed around the Lehmann model [Lehmann, 1959; Sato, Landisman, and Ewing, 1960]. In the Lehmann model (see Table 10) the shear-wave velocity increases slightly from the base of the crust to a depth of 120 km, where it drops discontinuously from 4.64 to 4.30 km/sec. The shear-wave velocity is taken as constant from a depth of 120 km to a depth of 220 km, where the velocity increases discontinuously to 4.71 km/sec. At greater depth the velocity distribution is that of the Jeffries-Bullen model of the earth. The average shear-wave velocity in the Lehmann model is greater than in the Gutenberg model, and the periods for the low-order oscillations are correspondingly lower. The Gutenberg model deviates from observations in having too short a

TABLE 15. Comparison of Observed and
Calculated Periods

Model	D
Gutenberg IV	0.026
Gutenberg II	0.044
Gutenberg V	0.074
Gutenberg I	0.080
Gutenberg III	0.096
Gutenberg low-density	0.113
Gutenberg	0.098
Gutenberg stiff	0.262
Lehmann velocity Bullen density	0.213
Lehmann III	0.257
Lehmann I	0.264
Lehmann II	0.270
Lehmann	0.270
Lehmann IV	0.280
Homogeneous	1.032
Homogeneous stiff	1.184

period when compared with observations; the Lehmann model therefore agrees with observations less well than the Gutenberg model.

A number of adjusted Lehmann models have been considered. The Lehmann I model is identical with the Lehmann model in the lower part of the mantle, but the discontinuity in shear-wave velocity is smoothed out so that the variation in shear-wave velocity is continuous. The shifts in resonant frequencies are slight (see Table 11).

The shear-wave velocity is assumed to remain constant to a depth of 350 km in Lehmann II. The density also remains constant over this region. At greater depths the shear-wave velocity is joined smoothly to the unadjusted Lehmann model. The periods of the low-order oscillations are decreased, since the average shear-wave velocity of Lehmann II is greater than that of the unadjusted Lehmann model.

The Lehmann III and Lehmann IV models represent slight modifications to the rigidity and density of the Lehmann model. In Lehmann III the rigidity is taken to be 2 per cent less than in the Lehmann model; in Lehmann IV, it is 2 per cent greater. The corresponding shift in the resonant frequencies is small.

In the final Lehmann model considered, the velocity is that of the Lehmann model but the rigidity is derived from Bullen's model B density distribution (see Table 11). This Lehmann model

gives the best fit to the observations, but it is not in as good agreement as the Gutenberg models (see Table 15).

Tables 11 to 14 also list the resonant frequencies for a homogeneous model and a Gutenberg model in which the lower boundary is assumed fixed. Maintaining a rigid core-mantle boundary increases the resonant frequencies of the low-order oscillations. In the case of $_0T_2$ for the Gutenberg model the resonant frequency is changed from 43.63 to 32.15 minutes. The shift in frequency due to the stiffness of the lower boundary decreases at the higher modes. This is illustrated in Figure 24, where the percentage shift $(\omega_S - \omega_F)/\omega_F$ (ω_S and ω_F are the resonant frequencies for a stiff and free core-mantle boundary, respectively) is given for the first few oscillations for the Gutenberg and homogeneous models. For $_0T_8$ the shift is less than 1 part in 1000. In the high-order oscillations the energy is concentrated toward the upper boundary, and any stiffness of the core-mantle interface does not perturb the toroidal oscillations.

The transition from a mantle with a free lower boundary to a stiff lower boundary has been studied by determining the resonant frequency of the Gutenberg model earth with an additional inner spherical shell 100 km thick.
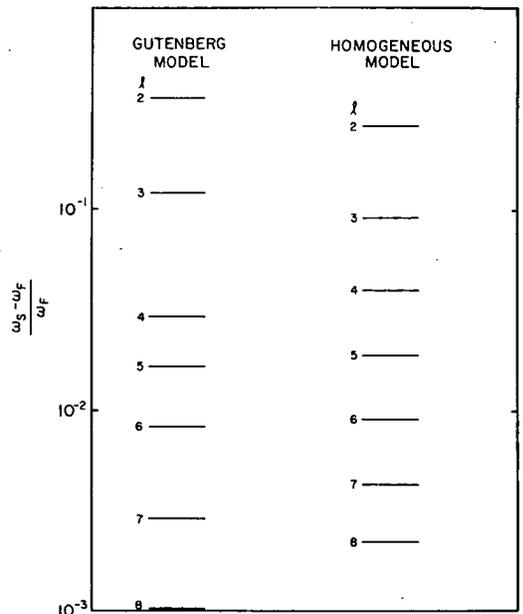
Fig. 24. Percentage shift in resonant frequencies due to rigid inner boundary.
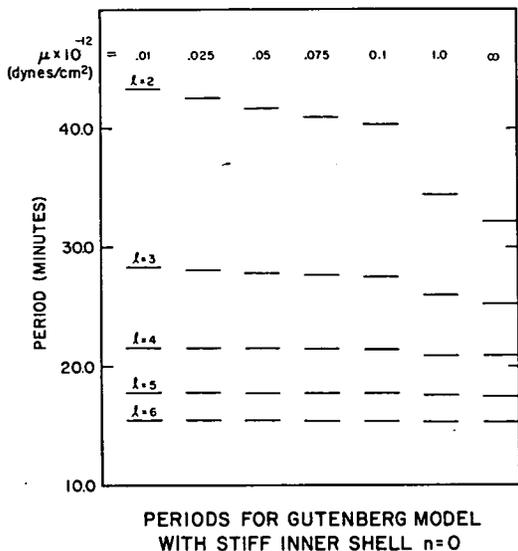
PERIODS FOR GUTENBERG MODEL
WITH STIFF INNER SHELL n=0

Fig. 25. Variation of resonant periods with rigidity of an additional 100-km-thick inner shell. Inner boundary of inner shell is rigid.

The shell is taken to have a density of 10, and the periods corresponding to various rigidities have been calculated. Figure 25 illustrates the case in which the additional inner shell is assumed to have a rigid inner boundary. If the rigidity of the inner shell is taken as 1×10^{10} dynes/cm^2, the period for the $_0T_2$ oscillations is 43.28 minutes, or about 1 per cent less than the period for the Gutenberg model without the additional inner shell. This calculation suggests that if the core had a rigidity of the order of 10^{10} dynes/cm^2 it would result in a measurable perturbation in the frequency of the $_0T_2$ oscillation. Figure 25 illustrates the variation in the periods as a function of the rigidity of the inner shell. The low-order oscillations have their periods shifted by a greater degree than the high-order oscillations, the effect for $l = 6$ being less than 1/1000.

Similar computations have been carried out assuming that a shell 100 km thick with a density of 10 is fastened to the lower mantle and that the inner boundary of the shell is kept free. If the rigidity of the inner shell is 1×10^{12} dynes/cm^2, somewhat less than the rigidity of the lower part of the mantle, the resonant periods are increased slightly. The increase for the $_0T_2$ oscillation is from 43.63 to 43.74 minutes. As the rigidity is increased above the value of the rigidity of the lower mantle, the boundary is stiffened and the corresponding frequencies of

oscillation are increased. This is illustrated in Figure 26, where the periods for the free inner shell are shown. Once again the effect of the inner shell on the resonant frequencies is greatest for the low-order oscillations and becomes negligibly small for the high-order oscillations.

7. ORIGIN OF THE LOW-VELOCITY LAYER

Study of the point of inflection of travel-time curves for earthquakes originating at various depths led *Gutenberg* [1948, 1953] to postulate the existence of a layer in the upper mantle having elastic wave velocities lower than the material above and below. This supported an earlier interpretation by *Gutenberg and Richter* [1939]. Gutenberg's early results were not universally accepted, and the general interpretation of the variation of velocity with depth was that based on the Jeffrey model for the upper mantle. In this model both the shear and compressional velocity increase monotonically with depth. In recent years, several detailed studies on the propagation of surface waves indicate the presence of a low-velocity zone under both continents and oceans. *Landisman and Sato* [1958] and *Press* [1959] studied the propagation of Love waves and G waves in the upper mantle. Investigations of mantle Rayleigh waves [*Takeuchi, Press, and Kobayashi*, 1959] provided additional
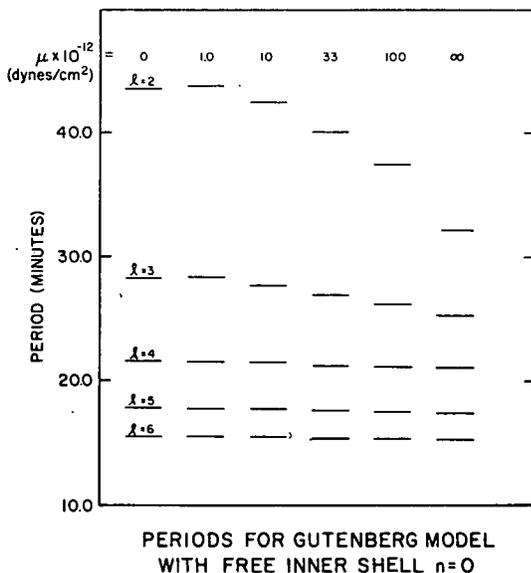
PERIODS FOR GUTENBERG MODEL
WITH FREE INNER SHELL n=0

Fig. 26. Variation of resonant periods with rigidity of a 100-km-thick inner shell. Inner boundary of inner shell is free.

supporting evidence for the presence of a layer of low velocity.

A number of workers have extended Gutenberg's results for near earthquakes [*Lehmann*, 1953; *Shirokova*, 1959]. The present study of the toroidal oscillations coupled with the work of *Alterman, Jarosch, and Pekeris* [1961] provides further confirmation for a region of lower velocity below the crust but in the upper 100 to 200 km of the earth.

Gutenberg's initial interpretation of the low-velocity layer was in terms of the asthenosphere of *Daly* [1940], which was a world-encircling layer of glassy material having little mechanical strength. Daly postulated this layer in order to explain both the world-wide occurrence of basalt and the mobility of the outer regions of the earth. In Gutenberg's view, the low-velocity region is composed of silicates at or near the melting point. *Press* [1959] states that it is not unreasonable to ascribe the low velocity to material near the melting point. If matter were near the melting point, it might be possible to account for the long-period nature of observed S waves by supposing that the high-frequency S waves were absorbed as a result of imperfect elasticity of the nearly molten material. Press also envisages the low-velocity layer as a source for primary basaltic magma and a zone where the lower mantle is decoupled from the crust for tectonic processes. *Birch* [1952] found it unnecessary to postulate the existence of a zone near melting to account for the low-velocity layer. In summarizing data on the variation of velocity with temperature and pressure, Birch noted that a low-velocity layer would result if the temperature gradient exceeded some 6° to 7°/km.

In the following paragraphs we examine the variation of S-wave velocity with temperature and pressure to determine whether a low-velocity zone could form in a layer that is chemically homogeneous on a large scale and is in hydrostatic equilibrium. The principal result of this study is that the temperature gradients to be expected in the upper mantle are more than sufficient to produce a decrease in S-wave velocity starting at the base of the crust and extending to a depth of 100 to 200 km. There is no need to suppose that the temperature closely approaches the melting temperature. These results support earlier theoretical treatments of the low-velocity layer [*Birch*, 1952; *Valle*, 1956].

The variation of the velocity of a shear wave, C_s, with radius r is

$$\frac{dC_s}{dr} = \left(\frac{\partial C_s}{\partial p}\right)_T \frac{dp}{dr} + \left(\frac{\partial C_s}{\partial T}\right)_p \frac{dT}{dr} \quad (46)$$

assuming the upper mantle to be chemically homogeneous. The upper mantle is assumed to be in hydrostatic equilibrium

$$dp = -\rho g \, dr$$

Writing the shear-wave velocity as

$$C_s = (\mu/\rho)^{1/2}$$

the variation is found to be

$$\frac{dC_s^2}{dr} = \left[\frac{1}{\rho}\left(\frac{\partial \mu}{\partial T}\right) + \frac{\alpha C_s^2}{\rho}\right]\frac{dT}{dr}$$
$$- g\left[\left(\frac{\partial \mu}{\partial p}\right) - \frac{C_s^2 \rho}{K_T}\right]$$

α is the coefficient of thermal expansion

$$\alpha = -(1/\rho)(\partial \rho/\partial T)_p$$

and K_T is the isothermal incompressibility

$$K_T = \rho[\partial p/\partial \rho]_T \approx K_s \quad (47)$$

K_s is the adiabatic incompressibility

$$K_s = \rho\left[C_P^2 - \frac{4}{3}C_s^2\right]$$

The ratio of the adiabatic incompressibility to the density is directly determined by the observed elastic-wave velocities.

Birch [1938] studied the variation of shear-wave velocity with pressure according to the theory of finite strain. One result of the theory is that the shear-wave velocity increases linearly with pressure

$$C_s^2 = C_s^{0^2}\{1 + (\rho/\mu K_T^0)(\lambda + 2\mu)\}$$

provided that the compression ratio for the material is much less than 1.

$$|\Delta\rho/\rho| \ll 1$$

C_s^0 is the zero pressure value of the shear velocity. Since

$$|\Delta\rho/\rho| \approx K_T^{-1}\rho$$

and since at a depth of 300 km the pressure is 10^5 bars (see Figure 27), we have

$$|\Delta\rho/\rho| < 1$$

down to this depth. It is to be expected that the
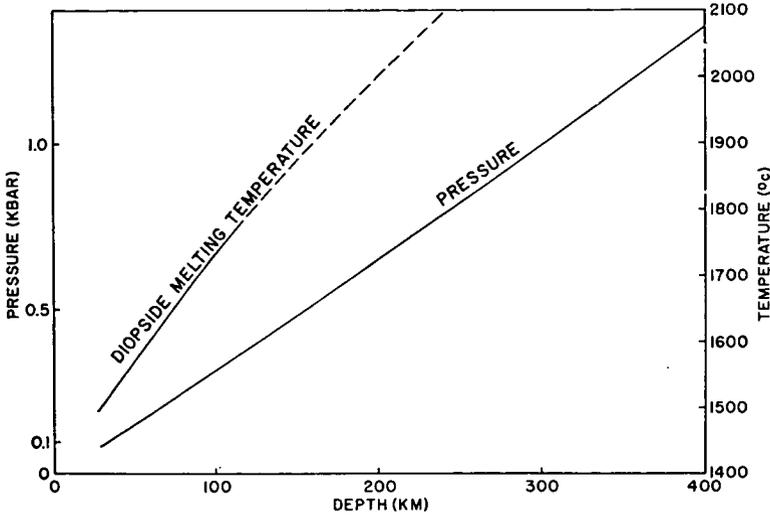
Fig. 27. Variation of pressure and melting point of diopside with depth in the upper mantle.
(Melting point of diopside after *Boyd and England* [1958].)

variation of velocity with pressure will not be linear at depths of 200 to 300 km. A further result from *Birch* [1938] is that the variation of compressional-wave velocity C_p is greater than the variation of the shear-wave velocity with pressure.

$$\left(\frac{\partial C_p^2}{\partial p}\right)\Big/\left(\frac{\partial C_s^2}{\partial p}\right) \cong \frac{13}{3} - \frac{4 C_s^{0^2}}{C_p^{0^2}}$$

No comparable theory of the variation of the shear-wave velocity with temperature is available.

A number of workers have shown that at moderate conditions of temperature and pressure an increase of temperature tends to decrease C_s, whereas an increase of pressure raises C_s. The results of *Hughes and Maurette* [1957] on gabbros and dunite are summarized in Table 16. The effect of pressure on velocity increases with increasing temperature. In a detailed study of the variation of frequency of torsional oscillations with temperature, *Birch* [1958] finds that, for gabbros,

$$\frac{1}{C_s}\frac{\partial C_s}{\partial T} = -6.0 \times 10^{-5}/\text{deg}$$

Because of the limited range over which the measurements of the variation of shear-wave velocity with temperature and pressure have been carried out it would be premature to attempt to directly extrapolate laboratory values

to conditions existing in the upper mantle. A further complicating factor is the uncertainty in the chemical composition of the material immediately below the Mohorovicic discontinuity. An alternative approach is suggested by the fact that temperature and pressure have opposite effects on the shear-wave velocity. Since C_s increases with increasing pressure, we can thus ask for the minimum temperature gradient required to compensate the effect of pressure and produce a decrease in C_s [*Birch*, 1952, 1958].

The condition that the shear-wave velocity decreases with increasing depth in a chemically homogeneous layer is

$$\left(\frac{\partial C_S}{\partial T}\right)_p \frac{dT}{dr} + \left(\frac{\partial C_S}{\partial p}\right)_T \frac{dp}{dr} = \frac{dC_S}{dr} > 0$$

$$\frac{dT}{dr} > \rho g \left(\frac{\partial C_S}{\partial T}\right)_p \Big/ \left(\frac{\partial C_S}{\partial p}\right)_T \qquad (48)$$

TABLE 16. $\partial C_s/\partial p$ in km/sec/bar after *Hughes and Maurette* [1957]
Pressure range 3000–6000 bars

Rock type	$\partial C_s/\partial p$	
	At 25°C	At 300 °C
San Marcos gabbro	8×10^{-6}	3×10^{-5} (400°C)
Bytownite gabbro	7×10^{-6}	3×10^{-5}
Dunite	2×10^{-5}	7×10^{-5}

TABLE 17.   Thermal Expansion of Possible Constituents of the Upper Mantle (10^6 deg^{-1})
After *Skinner* [1956] and *Birch* [1952]

Mineral	α at 298°K	α at 600°K	α at 1000°K	Debye Temperature from Heat Capacity, °K	Debye Temperature from Entropy, °K
Periclase MgO	23.7	39.6	44.2	739	745
Forsterite Mg_2SiO_4	25.2	36.5	43.0	873	760
Jadeite $NaAlSi_2O_6$	19.5	27.6	38.2	933	751
Pyrope $Mg_3Al_2(SiO_4)_3$	19.8	25.4	28.6		
Grossularite $Ca_3Al_2(SiO_4)_3$	16.4	23.0	27.1		
Almandite $Fe_3Al_2(SiO_4)_3$	15.7	23.6	29.4		

Since

$$\left(\frac{\partial C_S}{\partial T}\right)_p \Big/ \left(\frac{\partial C_S}{\partial p}\right)_T = -\left(\frac{\partial p}{\partial T}\right)_{C_S}$$

equation 48 can be written

$$\frac{dT}{dr} > -\rho g \left(\frac{\partial p}{\partial T}\right)_{\mu, \rho}$$

Now we approximate the change of pressure with temperature at constant density and rigidity by

$$\left(\frac{\partial p}{\partial T}\right)_\rho \approx \left(\frac{\partial p}{\partial T}\right)_{\mu, \rho} \qquad (49)$$

Equation 49 would hold exactly if the rigidity followed a law of corresponding states

$$\mu = f(\rho) \qquad (50)$$

There is no rigorous justification for equation 50, but various laboratory data suggest that some form of a corresponding state law holds among close-packed silicates. Under the approximation expressed in equation 50, and using (47), the temperature gradient required to produce a decrease in shear-wave velocity is

$$\frac{dT}{dr} > -\frac{g}{\alpha} \left(C_P{}^2 - \frac{4}{3} C_S{}^2\right)^{-1} \qquad (51)$$

The minimum temperature gradient required for decreasing C_S with depth is thus determined by seismic velocities and the coefficient of thermal expansion. Note that equation 51 is also the condition that the temperature gradient produces a density decreasing with depth.

The principal uncertainty in applying equation 51 is in the value of the thermal expansion. Table 17 lists representative values of the coefficient of thermal expansion for materials

that may be important constituents of the upper mantle. The available Debye temperatures are also listed.

The temperature variation of the thermal expansion decreases rapidly at temperatures in excess of the Debye temperature. The temperature at a depth of 50 km probably exceeds 800°K. We therefore assume that the variation of thermal expansion with temperature can be neglected in the region of 50 to 300 km.

The dependence of thermal expansion on pressure is more uncertain. The thermodynamic relation

$$\left(\frac{\partial \beta}{\partial T}\right)_p = -\left(\frac{\partial \alpha}{\partial p}\right)_T$$

provides a means of obtaining approximate values. The temperature coefficient of compressibility has been measured in the laboratory over a temperature range of some 200°. The value for forsterite is 1.4×10^{-10}/deg bar; for periclase, 1.8×10^{-10}/deg bar. If the variation of the thermal expansion with pressure were linear, the change in thermal expansion for a change of pressure of 10^6 bars would be about 0.2 the zero pressure value. The variation due to pressure over a pressure range of 10^6 bars is of the same magnitude as the variation among the different compositions listed in Table 17.

An approximate expression for the variation of the thermal expansion with pressure can be obtained from the theory of solids [*Birch*, 1952]. In the ionic theory of solids, the dimensionless quantity

$$\frac{K_T}{\alpha} \left(\frac{\partial \beta}{\partial T}\right) = \frac{-K_T}{\alpha} \left(\frac{\partial \alpha}{\partial p}\right) = a$$

varies from 4 to 8. The pressure dependence of

TABLE 18. Variation of Incompressibility in
Gutenberg Model of Upper Mantle

Depth, km	K_s/ρ, km/sec	K_s, bars $\times 10^6$	$-\alpha \dfrac{dT}{dr}$ km$^{-1} \times 10^4$	K_s, bars $\times 10^{-6}$ (Gutenberg low-density model)
33	38.42	1.28	2.55	1.29
50	38.30	1.28	2.56	1.28
60	38.42	1.29	2.55	1.29
70	38.49	1.29	2.55	1.29
80	38.60	1.30	2.53	1.29
90	38.39	1.30	2.55	1.29
100	37.41	1.27	2.62	1.25
125	36.39	1.24	2.69	1.22
150	36.90	1.27	2.65	1.24
175	38.11	1.32	2.57	1.28
200	39.56	1.38	2.47	1.34
225	40.88	1.43	2.40	1.39
250	42.74	1.51	2.29	1.47
300	45.10	1.61	2.17	1.59
350	47.32	1.71	2.07	1.71
400	49.85	1.84	1.97	1.84

the thermal expansion of periclase and forsterite can be accounted for by $a = 4$. Provided that pressure is small compared with the incompressibility, the decrease of thermal expansion with pressure is approximated by

$$\alpha = \alpha_0 \{1 - [a(p - p_0)/K_T]\} \qquad (52)$$

The minimum temperature gradient required to produce a low-velocity layer can be written as

TABLE 19. Critical Temperature Gradient in
Gutenberg Model of Upper Mantle

Depth, km	$\dfrac{4(p - p_{30})}{K_S}$	dT/dr, deg/km $\alpha_0 = 4.0 \times 10^{-5}$/deg	dT/dr, deg/km $\alpha_0 = 3.0 \times 10^{-5}$/deg
50	0.019	6.51	8.68
60	0.031	6.58	8.77
70	0.041	6.62	8.82
80	0.050	6.67	8.89
90	0.060	6.77	9.02
100	0.071	7.02	9.36
125	0.100	7.41	9.88
150	0.124	7.46	9.94
175	0.145	7.36	9.81
200	0.164	7.21	9.61
225	0.182	7.09	9.45
250	0.195	6.85	9.13
300	0.226	6.66	8.88

$$\frac{dT}{dr} > -\frac{g}{\alpha_0}\left(C_p{}^2 - \frac{4}{3} C_s{}^2\right)$$
$$\cdot \left(1 + \frac{a(p - p_0)}{K_T}\right) \qquad (53)$$

or

$$\frac{dT}{dr} > -\frac{2.6 \times 10^{-4}}{\alpha} \frac{\deg}{km}$$

A thermal expansion of 4×10^{-5}/deg leads to a temperature gradient of 6°/km. *Birch* [1952], considering laboratory values for the variation of velocity, estimated the critical temperature gradient as 6.6°/km.

Table 18 lists the product of the thermal expansion and temperature gradient required to produce a decrease of velocity with depth in the Gutenberg model of the upper mantle. The incompressibility of the Gutenberg low-density model consistent with equation 51 is also listed for comparison. The irregularities in the values in Table 18 undoubtedly reflect the uncertainties in the velocity distribution. The approximate form for the critical temperature gradient, equation 53, leads to the gradients listed in Table 19 for two values of the initial thermal expansion. These values for α_0 are representative of the range of high-temperature thermal expansions observed in silicates (see Table 16).

In Table 19 the correction term for the variation of thermal expansion with pressure has been calculated on the assumption that $a = 4$. As can be seen in the table, the maximum correction to the thermal expansion is 23 per cent

Fig. 28. Minimum temperature required to produce a low-velocity-zone temperature at 30 km is 460. The albite-jadeite plus quartz stability curve after *Birch and LeComte* [1960]; the quartz-coesite curve after *Boyd and England* [1960].

TABLE 20.   Temperature Gradients in
Model Earths

Temperature distribution at 4.5×10^9 years leads
to central temperature of 4000°C. Opacity is 10
cm⁻¹. Total radioactivity equals earth made up of
chondrites.

Model	Depth, km	Mean Temperature Gradient, deg/km
Radioactivity in upper 500 km	50	16
	150	6.5
	250	4.0
	350	2.8
	450	1.8
Radioactivity in upper 400 km	50	16
	150	6.2
	250	3.6
	350	2.2
	450	1.0
Radioactivity in upper 300 km	50	16
	150	5.8
	250	2.9
	350	1.1
	450	0.9
Radioactivity in upper 200 km	50	15
	150	4.9
	250	1.4
	350	1.2
	450	1.0
Radioactivity in upper 100 km	50	15
	150	2.1
	250	1.6
	350	1.3
	450	1.1

at a depth of 300 km and less than 12 per cent
down to the critical depth of 150 km.

The temperatures corresponding to the critical
temperature gradient listed in Table 19 are shown
in Figure 28 on the assumption that the tem-
perature at 30 km is 460°. In the Gutenberg
model the velocity decreases to a depth of 150
km and then begins to increase. This means that
to a depth of 150 km the critical temperature
gradient must be exceeded, and at depths greater
than 150 km the actual temperature gradient
must be less than the critical. In Figure 28 the
range of temperatures that might be expected
for depths between 50 and 150 km is indicated.
In addition to the minimum temperature curves,
the melting curve for diopside and the quartz-
coesite and albite-jadeite transition curves are
shown. The diopside melting temperature doubt-

less exceeds the fusion temperature of the
multicomponent mantle material. It can be seen
that in the depth range of 50 to 150 km the
temperature could assume values considerably
less than the melting point of diopside and still
satisfy the criteria for decreasing velocity with
depth. It should be emphasized that on the
Gutenberg model the temperatures to 150 km
are absolute minimum temperatures provided
that the temperature at 30 km is 460°. On this
basis it is seen that the minimum depth of
stability of coesite relative to quartz is 80 to
100 km, and that the minimum depth for the
stability of jadeite plus quartz relative to albite
is 60 to 75 km. Under the Gutenberg model and
with a temperature of 460° at 30-km depth,
neither of the high-pressure phases would be
stable at a depth of less than 60 km.

The limits on thermal conditions in the upper
mantle derived from the variations of velocity
with depth in the Gutenberg model of the upper
mantle can be compared with thermal conditions
calculated on assumed distribution of thermal
parameters [MacDonald, 1959, 1961].

MacDonald [1961] determined the development
of temperature within an earth with an initial
central temperature of 4000° and an initial
temperature of 2000° at 300-km depth. The
material composing the earth is assumed to
transport heat by radiation with an opacity of
10 cm⁻¹. The radioactivity corresponds to an
earth of chondritic composition. MacDonald
found that the models resulted in surface heat
flows 20 to 80 per cent in excess of the earth's
heat flow. In addition, models in which radio-
activity was concentrated at depths greater than
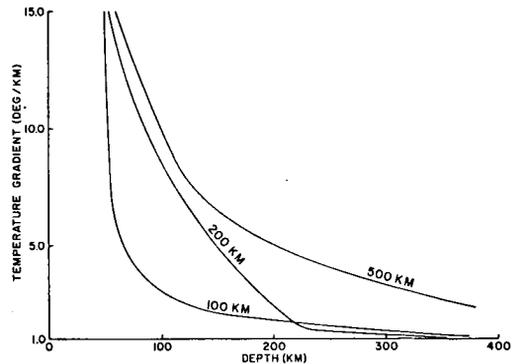
Fig. 29. Temperature gradient in upper mantle
with radioactivity concentrated in upper 500, 200,
and 100 km.

300 km led to temperatures in excess of melting temperature over substantial regions of the mantle. In these calculations no attempt was made to distinguish continental from oceanic crustal structure. Table 20 and Figure 29 give the temperature gradients obtained by MacDonald.

The thermal models listed in Table 20 assume a high initial temperature and low opacity. The combined effects of the high contribution of radiation to thermal conductivity plus the upward concentration of radioactivity lead to a high near-surface temperature gradient, tapering off at greater depths. If the models are taken literally the radioactivity must be concentrated to depths of at least 150 to 250 km in order to produce a thermal gradient sufficient for a low-velocity layer. The indicated requirements of radioactivity at depths of the order of 200 km depend sensitively on the assumed thermal conductivity. In the models, the conductivity at 200 km is reduced sharply because of the low opacity. A lower conductivity would allow a suitable temperature gradient for the low-velocity layer. It should also be noted that the thermal models listed in Table 20 lead to heat flows in excess of the observed heat flows. The high surface heat flow implies a higher temperature gradient than would exist in a model earth in which the radioactivity or the initial temperature was lower.

MacDonald [1959] discusses steady-state models having a lower surface heat flow and adjusted to represent oceanic and continental structures. In model 5 the temperature at 30 km was taken to be 460° (see Table 21). The heat flow at a depth of 30 km is one-half the surface heat flow of 52 ergs/cm²/sec. Model 5 is thus an attempt at modeling subcontinental conditions. The opacity is 30 cm⁻¹, a value 3 times higher than that assumed in the models listed in Table 20. Models 4 and 6 are roughly representative of suboceanic conditions. The temperature at 30 km is 420°, and the heat flow at 30 km equals the surface heat flow. The contribution of radioactivity above 30 km to the surface heat flow is assumed small compared with the total heat flow. In model 4 the conductivity is affected by an opacity of 30 cm⁻¹; in model 6 a greater contribution from radiation is assumed since the opacity is taken at 10 cm⁻¹.

The upward concentration of radioactivity in continental model 5 leads to low temperature gradients of the order of 9°/km. These gradients

TABLE 21. Temperature Gradient in Steady-State Earth Models

Model	Depth	Mean Temperature Gradient, deg/km
Model 5	50	9.0
Continental model with	100	7.1
chondritic radioactivity	150	5.2
in upper 430 km; heat	200	3.6
flow at 30 km = 26.1	250	2.6
ergs/cm²/sec; ϵ_0 = 30	300	1.8
cm⁻¹; T at 30 km =	350	1.0
460°C	400	0.6
Model 4	50	18
Oceanic model with	100	12
chondritic radioactivity	150	7.5
in upper 430 km; heat	200	5.0
flow at 30 km = 54	250	3.4
ergs/cm²/sec; ϵ_0 = 30	300	2.4
cm⁻¹; T at 30 km =	350	1.4
420°C	400	0.6
Model 6	50	15
Oceanic model; same	100	8.2
as model 4 with	150	5.0
ϵ_0 = 10 cm⁻¹	200	3.2
	250	2.2
	300	1.4
	350	1.0
	400	0.6

are lower than the gradients at the same depth under oceanic areas because of the absence of marked upward concentration of radioactivity in oceanic areas. The upward concentration of radioactivity in continental areas implies that the low-velocity layer under continents should not be as marked or extend to as great a depth as under oceans. In both cases we should expect the low-velocity layer to commence immediately below the crust. Under oceans the low-velocity layer should extend to depth of 100 to 150 km; under continents, it might not extend beyond 100 km.

Even though the details of the velocity and temperature distribution on the continents and oceans are most uncertain, several firm qualitative statements can be made. A low-velocity layer should be expected, provided that the upper mantle is homogeneous on a large scale. The dominance of the temperature effect over the effect of increasing pressure implies a low-velocity layer extending to depths of 100 to 150

km in a homogeneous material. The temperature need not approach the melting temperature for a low-velocity layer to exist. If the subcrustal layer is homogeneous on a large scale, and if a low-velocity layer exists, the low-velocity layer must begin at the Mohorovicic discontinuity. Indeed, this is what *Gutenberg* [1959b] has suggested in one of his last public statements on the low-velocity layer. If, on the other hand, it is found on detailed study that the low-velocity layer does not begin at the base of the crust, some large-scale inhomogeneity in the upper layers of the mantle is implied.

The mere existence of the low-velocity layer has important implications about the thermal nature of the upper mantle. It would appear that the thermal conductivity of the material making up the upper mantle must be less than that implied by using an opacity of 10 cm^{-1} in evaluating the radiative contribution to the thermal conductivity. Furthermore, if the low-velocity layer extends to 150 km or more, substantial heat sources must persist to this depth or to greater depths. As has been pointed out elsewhere [*MacDonald*, 1961], this depth of burial of the radioactivity implies a low initial temperature for the earth or a lower bulk radioactivity than that of chondritic meteorites or both.

REFERENCES

Alsop, L. E., G. H. Sutton, and M. Ewing, Free oscillations of the earth observed on strain and pendulum seismographs, *J. Geophys. Research*, 66, 631–641, 1961a.

Alsop, L. E., G. H. Sutton, and M. Ewing, Measurement of Q for very long period free oscillations, *J. Geophys. Research, 66*, in press, 1961b.

Alterman, Z., H. Jarosch, and C. L. Pekeris, Oscillations of the earth, *Proc. Roy. Soc. London, A, 252*, 80–95, 1959.

Alterman, Z., H. Jarosch, and C. L. Pekeris, Propagation of Rayleigh waves in the earth, *Geophys. J.*, 1961.

Backus, G., and F. Gilbert, The rotational splitting of the free oscillations of the earth, *Proc. Nat. Acad. Sci. U. S., 47*, 362–371, 1961.

Benioff, H., J. C. Harrison, L. LaCoste, W. H. Munk, and L. B. Slichter, Searching for the earth's free oscillations, *J. Geophys. Research, 64*, 1334–1337, 1959.

Benioff, H., F. Press, and S. Smith, Excitation of the free oscillations of the earth by earthquakes, *J. Geophys. Research, 66*, 605–619, 1961.

Birch, F., The effect of pressure upon the elastic properties of isotropic solids, according to Murnaghan's theory of finite strain, *J. Appl. Phys., 9*, 279–288, 1938.

Birch, F., Elasticity and constitution of the earth's interior, *J. Geophys. Research, 57*, 227–286, 1952.

Birch, F., Interpretation of the seismic structure of the crust in the light of experimental studies on wave velocities in rocks, in *Contributions to Geophysics*, pp. 158–170, Pergamon Press, New York, 1958.

Birch, F., and P. L. LeComte, Temperature-pressure plane for albite composition, *Am. J. Sci., 258*, 209–217, 1960.

Blackman, R. B., and J. W. Tukey, *The Measurement of Power Spectra*, Dover Publications, New York, 1958.

Bogert, B. P., An observation of free oscillations of the earth, *J. Geophys. Research, 66*, 643–646, 1961.

Boyd, F. R., and J. L. England, Melting of diopside under high pressure, *Carnegie Inst. Wash. Year Book 57*, 173, 1958.

Boyd, F. R., and J. L. England, The quartz-coesite transition, *J. Geophys. Research, 65*, 749–756, 1960.

Bullard, E., and H. Gellman, Homogeneous dynamos and terrestrial magnetism, *Phil. Trans. Roy. Soc. London, A, 247*, 213–278, 1954.

Bullen, K. E., *An Introduction to the Theory of Seismology*, Cambridge University Press, 1959.

Cowling, T., *Magnetohydrodynamics*, Interscience Publishers, New York, 1957.

Daly, R. A., *Strength and Structure of the Earth*, Prentice-Hall, New York, 1940.

Dorman, J. M., M. Ewing, and J. Oliver, Study of shear velocity distribution in the upper mantle from Rayleigh waves, *Bull. Seismol. Soc. Am., 50*, 87–116, 1960.

Elsasser, W. M., Hydromagnetic dynamo theory, *Revs. Modern Phys., 28*, 135–163, 1956.

Gilbert, J. F., and G. J. F. MacDonald, Free Oscillations of the earth, I, Toroidal oscillations, *J. Geophys. Research, 65*, 675–693, 1960.

Gutenberg, B., On the layer of relatively low wave velocity at a depth of about 80 kilometers, *Bull. Seismol. Soc. Am., 38*, 121–148, 1948.

Gutenberg, B., Wave velocities at depths between 50 and 600 km., *Bull. Seismol. Soc. Am., 43*, 223–232, 1953.

Gutenberg, B., *Physics of the Earth's Interior*, Academic Press, New York, 1959a.

Gutenberg, B., Wave velocities below the Mohorovicic discontinuity, *Geophys. J., 2*, 348–352, 1959b.

Gutenberg, B., and C. F. Richter, New evidence for a change in physical conditions at depths near 100 kilometers, *Bull. Seismol. Soc. Am., 29*, 531–537, 1939.

Hide, R., and P. H. Roberts, Hydromagnetic flow due to an oscillating plane, *Revs. Modern Phys., 32*, 799–806, 1960.

Hughes, D. S., and C. Maurette, Variation of elastic wave velocities in basic igneous rocks

with pressure and temperature, *Geophysics, 22,* 23–31, 1957.

Jeffreys, H., *The Earth,* Cambridge University Press, 1952.

Kakutani, T., Effect of a transverse magnetic field on the flow due to an oscillating flat plate, *Proc. Phys. Soc. Japan, 13,* 1504–1509, 1958.

Landisman, M., and Y. Sato, Shear wave velocities in the upper mantle (abstract) *Trans. Am. Geophys. Union, 39,* 522, 1958.

Lehmann, I., *P* and *S* at distances smaller than 25°, *Trans. Am. Geophys. Union, 34,* 477–483, 1953.

Lehmann, I., Velocities of longitudinal waves in the upper part of the earth's mantle, *Ann. géophys., 15,* 93–118, 1959.

Lin, C. C., Note on a class of exact solutions in magneto-hydrodynamics, *Arch. Ratl. Mech. Anal., 1,* 391–395, 1958.

Love, A., *A Treatise on the Mathematical Theory of Elasticity,* Dover Publications, New York, 1927.

Ludford, G. S. S., Rayleigh's problem in hydromagnetics: the impulsive motion of a pole-piece, *Arch. Ratl. Mech. Anal., 3,* 14–27, 1959.

Lyttleton, R. A., *The Stability of Rotating Liquid Masses,* Cambridge University Press, 1953.

MacDonald, G. J. F., Calculations on the thermal history of the earth, *J. Geophys. Research, 64,* 1967–2000, 1959.

MacDonald, G. J. F., The transport of heat in the earth, in *Vanuxem Lectures,* edited by H. H. Hess, Princeton University Press, 1961.

Martin, M., Frequency domain applications in data processing, *Gen. Elec. M.O.S.D., Tech. Information ser. 57SD340,* 1957.

Minorsky, N., *Introduction to Non-Linear Mechanics,* J. W. Edwards, Ann Arbor, 1947.

Morse, P. M., and H. Feshbach, *Methods of Theoretical Physics,* McGraw-Hill Book Co., New York, 1953.

Munk, W., and G. J. F. MacDonald, *The Rota-*

tion of the Earth, Cambridge University Press, 1960.

Ness, N. F., J. C. Harrison, and L. B. Slichter, Observations of the free oscillations of the earth, *J. Geophys. Research, 66,* 621–629, 1961.

Pekeris, C. L., Z. Alterman, and H. Jarosch, Comparison of theoretical with observed values of the periods of free oscillations of the earth, *Proc. Natl. Acad. Sci. U. S., 47,* 91–98, 1961.

Press, F., Some implications on mantle and crustal structure from *G* waves and Love waves, *J. Geophys. Research, 64,* 565–568, 1959.

Rikitake, T., Growth of the magnetic field of the self-exciting dynamo in the earth's core, *Bull. Earthquake Research Inst. Tokyo Univ., 33,* 571–582, 1955.

Sato, Y., M. Landisman, and M. Ewing, Love waves in a heterogeneous spherical earth, *J. Geophys. Research, 65,* 2395–2398, 1960.

Shirokova, E. I., Some facts on the character of the velocity change in the upper layers of the earth's mantle, *Izvest. Akad. Nauk SSSR, Geophys. Ser.,* 1127–1137, 1959.

Skinner, B. J., Physical properties of end members of the garnet group, *Am. Mineralogist, 41,* 428–436, 1956.

Stratton, J., *Electromagnetic Theory,* McGraw-Hill Book Co., New York, 1941.

Takeuchi, H., F. Press, and N. Kobayashi, Rayleigh wave evidence for the low-velocity zone in the mantle, *Bull. Seismol. Soc. Am., 49,* 355–364, 1959.

Tozer, D. C., The electrical properties of the earth's interior, pp. 414–436 in *Physics and Chemistry of the Earth, III,* McGraw-Hill Book Co., New York, 1960.

Valle, P. E., Sul gradiente di temperature necessarie per la formazion di 'low velocity layers,' *Ann. geofis., 9,* 371–378, 1956.